DISCLAIMER FOR FRONT PAGE OF MATERIALS TO BE MADE AVAILABLE VIA ETI INTERNET SITE

1. "Save to the extent set out in paragraph 2 below, this document and its contents are made available to you via the ETI's Internet Site "as is" without any representations, conditions, warranties or other assurance of any kind. The ETI and the authors, together with their employees, directors, servants or agents exclude to the maximum extent permissible by law all representations, warranties, conditions or other assurance whatsoever (whether express or implied) regarding the use of this document or its content including any warranties of title, merchantability, accuracy, completeness, non-infringement or that the document or its contents are of satisfactory or any particular quality or fit for any particular purpose. Any person accessing this document and using it or any of its contents accepts all risk in doing so.
2. Notwithstanding any statement to the contrary contained on the face of this document, the ETI confirms that the authors of the document have consented to its publication by the ETI."

Report ReDAPT MD1.3

S.Rolfo, J. McNaughton, T. Stallard, D. Apsley and P. Stansby

24th August 2012

Contents

Nomenclature

Capital Roman Symbols

A & B Constants for the definition of a generic boundary condition (see Eq. (10))

C_D Drag coefficient

C_L Lift coefficient

C_P Power coefficient

C_{pr} Pressure coefficient (see Eq. (42) for definition in case of rotating frame)

C_T Thrust coefficient

$\underline{S}_F$ Surface vector $= (S_1, S_2, S_3)$

T Period

Lower-case Roman Symbols

c Celerity or crest velocity

$\underline{e}_1$ Standard basis with $i = 1, 2, 3$

$\underline{g}$ Gravity vector $= (g_1, g_2, g_3)$

k Wave number $= 2\pi/\lambda$

$\dot{m}$ Mass flow rate

$\underline{n}$ Normal to the face vector $= (n_1, n_2, n_3)$

p Pressure

$\underline{u}$ Fluid velocity vector $= (u_1, u_2, u_3)$

$\underline{u}_w$ Wave induced velocity

$\underline{w}$ Mesh velocity vector $= (w_1, w_2, w_3)$

Capital Greek Symbols

Δt Time step

∇ Nabla operator $e_1 \partial_i$

Ω Cell volume

Lower-case Greek Symbols

η Free surface elevation (see Eqs. (22) and (26))

λ Wave lenght

$\underline{\underline{\lambda}}$ Mesh viscosity tensor

ω Angular frequency $= 2\pi/T$

Abbreviations

ALE Arbitrary Lagrangian Eulerian

BC Boundary condition

CFL	Courant–Friedrichs number $U\delta t/\Delta x$
FS	Free surface
LHS	Left Hand Side (linear system)
MPI	Message passage interface
Re	Reynolds number $= \rho UD/\mu$
RHS	Right Hand Side (linear system)
SF	Sliding interface

1 Introduction

This report explains the work undertaken in order to complete milestone MD1.3 of the modelling (MD) package of the ReDAPT project. The specific milestone for the CFD work under the framework of the ReDAPT project are summarised in Table 1. The tasks for this specific report are emphasised in bold and the major items are also underlined. The structure of this report is as follows:

- Description and validation of the ALE module in *Code_Saturne* in Sec. 2.2.1. The description also highlights differences between the ALE in V_2.0 and the new intermediate version V_2.2. Based on these differences, a new ALE implementation under V_2.0 has been also implemented that imports some of the beneficial features of V_2.2 into V_2.0. The reason of such new implementation is that the transfer of the sliding mesh module into V_2.2 will require a large effort;
- Description of a new parallel implementation of the sliding mesh module in order to increase parallel performances of the method and meet the requirements necessary for calculations on HPC machines (High Performing Computing) (see Sec. 3);
- Testing of the sliding mesh module with a free surface moving flow (see Sec 4) using a regular wave passing over a rotating cylinder;
- 3D simulation of the TGL turbine, including nacelle and support mast, with a fixed surface. This includes development of a mesh suitable for the TGL 1 MW turbine geometry (see Sec. 5) as provided in CAD form by TGL. The calculations are performed using Reynolds Average Navier-Stokes (RANS) equations to take into account the effect of turbulence. A uniform flow speed of 1.5 m/s is considered and power and thrust coefficients are compared to existing numerical predictions of TGL turbine performance;
- 3D simulation of the TGL turbine and associated structure with a free surface and with imposed regular waves and moving free surface. The wave conditions considered are representative of the EMEC site in terms of period and height.

MD1.1	Ideal turbine geometry Imposed rotation of a single cylindrical mesh (Coriolis forces or ALE) RANS Turbulence Report to identify development necessary for sliding mesh
MD1.2	Ideal turbine geometry Rotation using sliding mesh (with method description) RANS and LES turbulence No waves
MD1.3 (Actual Report)	**Real turbine geometry** **Waves (with description of the ALE method)** **RANS turbulence** **Sliding mesh**
MD1.4	Real turbine geometry Sliding mesh LES turbulence Waves Comparison of loads, and numerical flow field with field data

Table 1: Milestones for the CFD work in the ReDAPT project.

2 ALE module in *Code_Saturne*

Earlier ReDAPT work (MD1.1 and 1.2) focused on implementation of a sliding mesh method in *Code_Saturne* V_2.0. This employs several of the subroutines of the ALE method. Since ReDAPT MD1.2, *Code_Saturne* V_2.2 has been released which includes a modified implementation of the ALE method. Further code development would be required to implement the sliding mesh method in *Code_Saturne* V_2.2. In this section the main features of a free-surface of ALE method are introduced, the two *Code_Saturne* ALE versions are briefly compared and developments are explained for simulating free-surface waves above a bluff body.

2.1 Motivation

According to Ferziger and Peric (1997) three main options are available to simulate free surface flow:

1. Interface capturing methods: where the calculation is performed on a fixed grid. In this case the computational domain extends beyond the free surface and its shape is evaluated using a fluid-containing fraction, which represents the amount of fluid at each cell near the interface. An example of this group is the technique called volume-of-fluid (VOF), where an extra transport equation is solved for the fraction of cell occupied by the liquid phase (Hirt and Nichols, 1981). A second example is the marker-and-cell (MAC) method, where the free surface is traced by following the particle motion at the interface (Harlow and Welch, 1965). Generally these methodologies are very robust, but they are not very effective in simulating sharp interfaces and for free surfaces that are rapidly changing in time and space. Indeed a very fine mesh is required and *a priori* information, about the position and the elevation of the free surface, are mandatory.

2. Interface tracking methods: where the mesh is dynamically adapted to conform to the surface at all times (i.e. cells always contain fluid only) and consequently boundary faces are impermeable solids or free surfaces. These methods generally use moving mesh techniques such as the arbitrary Lagrangian-Eulerian (ALE). Examples of application of ALE with finite volume (FV) are given in Thé et al. (1994) and Mayer et al. (1998).

3. Mesh-less methods: where the equation of motion are no longer discretised on a mesh. A classical example is the so-called smooth-particle hydrodynamics (SPH), where the fluid is divided into a set of discrete particles. These particles have a spatial distance, over which their properties are "smoothed" by a kernel function. As a consequence the physical quantity of any given particle can be obtained by summing the relevant properties of all the particles that reside inside the support of the kernel (Gingold and Monaghan, 1977).

Code_Saturne used an interface tracking method in conjunction with ALE for the moving mesh. ALE capabilities have been already present in *Code_Saturne* since the early development of the code (Archambeau et al., 2004), whereas free surface module has been implemented subsequently (Cozzi, 2010). More recently *Code_Saturne* has been subjected to a major re-visitation and consequently both ALE and free-surface modules have been largely rewritten (Ferrand, 2011) in V_2.2. This section highlights some main code modifications and provides a comparison between the two versions of the ALE and free-surface modules for some simple test cases.

2.2 General overview of *Code_Saturne*

The Navier-Stokes equations for a Newtonian fluid in the case of a moving domain read:

$$\left\{ \begin{array}{rcl} \dfrac{\partial}{\partial t}(\rho \underline{u}) + (\underline{u} \otimes \rho\ (\underline{u} - \underline{w})) & = & \mathrm{div}\left(\underline{\underline{\sigma}}\right) + \rho \underline{g} \\ \dfrac{\partial \rho}{\partial t} + \mathrm{div}\left(\rho\,(\underline{u} - \underline{w})\right) & = & \Gamma \end{array} \right. \tag{1}$$

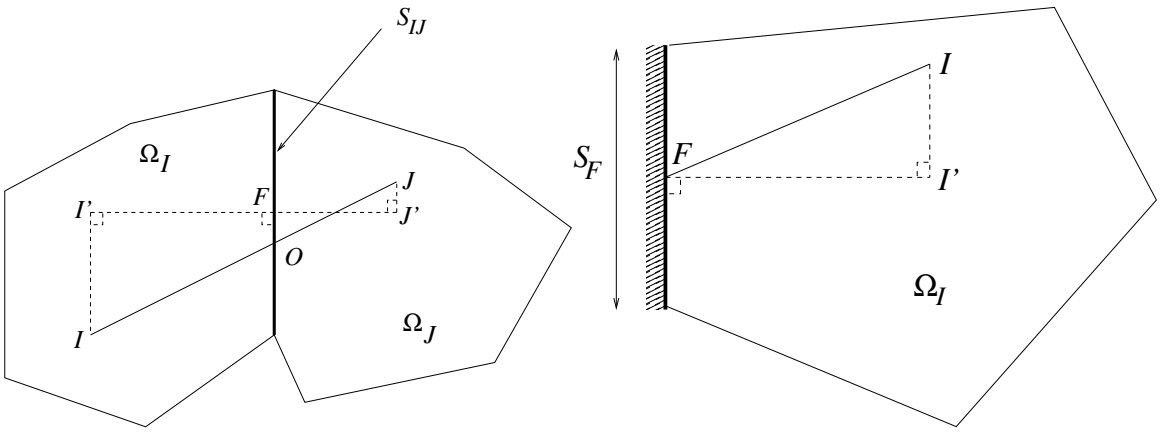

Figure 1: Outline of the internal and boundary faces in *Code_Saturne*

where ρ the density, $\underline{u}$ is the fluid velocity vector, $\underline{w} = \partial \underline{x}/\partial t$ is the mesh velocity vector, $\underline{g}$ the gravity vector and Γ an eventual mass source term. The stress tensor $\underline{\underline{\sigma}}$ can be decomposed into an isotropic and deviatoric part as follows:

$$\underline{\underline{\sigma}} = -p\underline{\underline{1}} + \underline{\underline{\tau}} = -p\underline{\underline{1}} + \mu\left(\nabla\underline{u} + (\nabla\underline{u})^T - \frac{2}{3}\mathrm{tr}\,(\nabla\underline{u})\,\underline{\underline{1}}\right) \tag{2}$$

The mesh velocity is arbitrary but must satisfy the boundary conditions, which can be divided into two types: (a) imposed mesh velocity and (b) sliding. More details about boundary conditions are provided below in Sec. 2.2.2. Particular care has also to be taken in order to conserve the volume and uniform fields. This condition is known as Geometric Conservation Law (GCL) and can be expressed as:

$$\frac{d}{dt}\int_{\Omega_I(t)} d\Omega = \int_{\Omega_I(t)} \mathrm{div}\,(\underline{w})\,d\Omega \tag{3}$$

where Ω is the cell volume. Verification of the GCL have been performed by Cozzi (2010) for V_2.0 by Ferrand (2011) for V_2.2 in case of conservation of a uniform velocity field on a random mesh deformation, with both reporting good approximation of Eq. (3).

2.2.1 ALE with Free Surface Boundary Condition

The choice of *Code_Saturne* for the mesh velocity is a Laplace equation, which reads:

$$\mathrm{div}\left(\underline{\underline{\lambda}}\nabla\underline{w}\right) = 0 \tag{4}$$

where $\underline{\underline{\lambda}}$ is the mesh viscosity tensor that in general is equal to the unitary matrix. At the free surface a simple condition of homogeneous Neumann is applied for all the variables with the exception of the pressure that is imposed. In case of the mesh velocity $\underline{w}$ the kinematic boundary condition is used at the free-surface and reads:

$$\underline{w}\cdot\underline{n}|_{FS} = \underline{u}\cdot\underline{n}|_{FS} \text{ or } \dot{m}_{FS} = 0 \tag{5}$$

with $\underline{n}$ being the normal to the face. In most applications the mesh is allowed to move only in the vertical direction (i.e. x_3), therefore the kinematic BC can be rewritten as:

$$w_3 = \frac{\underline{u}\cdot\underline{S}_F}{\underline{e}_3\cdot\underline{S}_F} \tag{6}$$

where $\underline{S_F}$ is the surface vector.

Implementation in *Code_Saturne*. At this point it is useful to give some details about differences between V_2.0 and V_2.2. One major difference between the two versions is that V_2.2 introduces a coupled solver for the resolution of a tensor (i.e. the velocity $\underline{u}$ or $\underline{w}$). This allows the full or partial implicitation of some terms (i.e. a Coriolis source term) and boundary conditions (i.e. symmetry). Indeed along with this modification the ALE module had been subjected to a major re-implementation. The following two algorithms present the procedure employed for the implementation of the ALE module with free surface in both versions.

Algorithm 1 Implementation of the ALE module with free surface in *Code_Saturne* V_2.2

for n to $n+1$ **do**
- Compute total mass flux $\rho\left(\underline{u}-\underline{w}\right)_f^n.\underline{S}^n$
- Compute the predicted velocity $\underline{\widetilde{u}}_I^{n+1}$ on Ω^n
- Compute the pressure corrected velocity $\underline{u}_I^{n+1}$ on Ω^n
- Compute mass flux $\underline{u}_f^{n+1}.\underline{S}^n$
- Compute $\underline{w}_I^{n+1}$ with free-surface BCs $\underline{u}_f^{n+1}.\underline{S}^n$
- Reconstruction mesh velocities at nodes $\underline{w}_N^{n+1}$
- Update the mesh from Ω^n to Ω^{n+1} with $\underline{w}_N^{n+1}$

end for

Algorithm 2 Implementation of the ALE module with free surface in *Code_Saturne* V_2.0

for n to $n+1$ **do**
- Compute total mass flux $\rho\left(\underline{u}-\underline{w}\right)_f^n.\underline{S}^n$
- Compute $\underline{w}_I^{n+1,m=1}$ with free-surface BCs $\underline{u}_f^n.\underline{S}^n$
- Compute the predicted velocity $\underline{\widetilde{u}}_I^{n+1}$ on Ω^n
- Compute the pressure corrected velocity $\underline{u}_I^{n+1}$
- Compute mass flux $\underline{u}_f^{n+1,m=1}.\underline{S}^n$
- **while** $\dot{m}_{FS}^{n+1,m} > \varepsilon_{FS}$ **and** $n_{FS} \leq n_{FS,MAX}$ **do**
  - Compute $\underline{w}_I^{n+1,m+1}$ with free-surface BCs $\underline{u}_f^{n+1,m}.\underline{S}^n$
  - Compute the predicted velocity $\underline{\widetilde{u}}_I^{n+1,m+1}$ on Ω^n
  - Compute the pressure corrected velocity $\underline{u}_I^{n+1,m+1}$ on Ω^n
  - Compute mass flux $\underline{u}_f^{n+1,m+1}.\underline{S}^n$
- **end while**
- Reconstruction mesh velocities at nodes $\underline{w}_N^{n+1,m+1}$
- Update the mesh from Ω^n to Ω^{n+1} with $\underline{w}_N^{n+1,m+1}$

end for

As it is obvious from Algorithm 1 and 2 the main difference is the stage at which the ALE is resolved: in V_2.0 this is done before the resolution of the NS equations, whereas in V_2.2 is done after. Another major difference is also the introduction of a coupled solver that is also used to solve $\underline{w}$. *Code_Saturne* solves for mesh velocity at the cell centre I, whereas the mesh movement is performed at the node N. Consequently $\underline{w}$ has to be interpolated from the cell centre to the node. This interpolation process is different between the two versions of *Code_Saturne*. In the case of V_2.0 we can define a support $\mathcal{F}_N$, that include all the faces sharing the same node N, and the interpolated mesh velocity $\underline{w}$ at node N reads:

$$\underline{w}_N = \frac{1}{n_F}\left(\sum_{\mathcal{F}_\mathcal{I}\in\mathcal{F}_N}\frac{1}{2}\left(\underline{w}_I+\underline{w}_J\right)+\sum_{\mathcal{F}_\mathcal{B}\in\mathcal{F}_N}\left(\underline{A}+\underline{\underline{B}}\,\underline{w}_I\right)\right) \tag{7}$$

where n_F is the total number of faces that are sharing the node N, $\mathcal{F}_\mathcal{I}$ is the part of the support composed by internal faces and $\mathcal{F}_\mathcal{B}$ is the part of the support composed by boundary faces.

On the other hand V_2.2 distinguish between nodes located at the boundaries and internal nodes. In case of a node located in the middle of the domain a support $\mathcal{C}_N$ that includes all the

cells that are sharing the node N is defined and the interpolation reads:

$$\underline{w}_N = \frac{\sum_{I \in \mathcal{C}_N} \frac{1}{\Omega_I} \left(\underline{w}_I + (\nabla \underline{w})_I \cdot \underline{IN} \right)}{\sum_{I \in \mathcal{C}_N} \frac{1}{\Omega_I}} \tag{8}$$

while for a node belonging to a boundary face a new support $\mathcal{F}_N$ is defined, which include all the faces sharing the same node N and the interpolation becomes:

$$\underline{w}_N = \frac{\sum_{F \in \mathcal{F}_N} \frac{1}{S_F} \left(\underline{w}_F + (\nabla \underline{w})_I \cdot \underline{FN} \right)}{\sum_{F \in \mathcal{F}_N} \frac{1}{S_F}} \tag{9}$$

It has to be noticed that in the above formulation the gradient of the mesh velocity at the adjacent to the face cell centre has been used, since the Jacobian matrix is not known at the face.

As already mentioned the main difference between the two ALE loops in V_2.0 and V_2.2 is the positioning of the ALE module. The placement of the ALE module before the resolution of the Navier-Stokes equations implies a loop in order to have a zero mass flux at the moving boundary. This configuration is not optimal since an extra loop between prediction and correction of the velocity is also present. Generally in the standard version of *Code_Saturne* only one correction stage is performed, but in the case of the sliding mesh module (see deliverable MD1.2) several iterations of predictions and corrections are mandatory, creating de facto two concatenated loop. This solution is not optimal, is computationally expensive and can be "easily" overcome using a solution strategy like the one presented in algorithm 1.

Therefore a new ALE module with free surface has been implemented in V_2.0 following algorithm 1 (mesh velocity resolution placed after the pressure corrector stage) but using the features of the ALE of V_2.0, which means $\underline{w}$ solved with a segregated solver and interpolated at the node using Eq. (7). This development ensures that the ALE method in V_2.0 benefits from the performance gains of the V_2.2 ALE method but can be used with the sliding mesh method that has been implement in V_2.0.

2.2.2 Boundary conditions

Boundary conditions are necessary to evaluate several terms like the convective one and the diffusive one. Indeed in case of skewed mesh the BCs are also necessary for the evaluation of gradients. *Code_Saturne* converts any type of BC into the following form:

$$\phi_F = A + B\phi_{I'} \tag{10}$$

where ϕ is a generic variable with a boundary face value of ϕ_F. I' is the projection of the cell centre on the normal to the face passing through the face centre F (see Fig. 1). A and B are two constants and their values depends on the type of BC imposed. The first advantage of this formulation is that any type of BC (i.e. Neumann or Dirichlet or Robin) can be decomposed into the formalism of Eq. (10) varying only A and B. The second important point is that B can be taken implicit (i.e. B can be add on the main diagonal of the matrix on the LHS). In case of a simple Dirichlet condition the values of A and B becomes:

$$A = \phi_{imposed} \text{ and } B = 0 \tag{11}$$

whereas in the case of a simple Neumann the values reads

$$q = \Gamma \frac{\partial \phi}{\partial n} \Rightarrow A = 0 \text{ and } B = \frac{q\,\overline{I'F}}{\Gamma} \tag{12}$$

In case of a tensor Eq. (10) takes a vectorial form as:

$$\underline{\phi}_F = \underline{A} + \underline{\underline{B}}\,\underline{\phi}_{I'}$$

Kinematic BC The kinematic BC of Eqs. (5) and (6) is imposed as a simple Dirichlet condition and therefore:

$$\underline{A} = \underline{g}\frac{\dot{m}_{FS}}{\rho\left(\underline{g}\cdot\underline{S}_F\right)} \text{ and } \underline{\underline{B}} = \underline{\underline{0}} \tag{13}$$

It is interesting to notice that with this formulation the free surface is allowed to move only in the direction of gravity, whereas the other components are kept equal to zero.

Sliding BC The condition of a sliding interface is the analogue of a symmetric BC for the mesh velocity $\underline{w}$ and in its vectorial form reads:

$$\begin{cases} \left.\dfrac{\partial\left(\underline{w}-\underline{w}\cdot\underline{n}\,\underline{n}\right)}{\partial n}\right|_{SF} = 0 \\ \underline{w}\cdot\underline{n}|_{SF} = 0 \end{cases} \tag{14}$$

where SF stands for sliding face. In case of a coupled solver this BC can be taken completely implicitly with the values:

$$\underline{A} = \underline{0} \text{ and } \underline{\underline{B}} = \underline{\underline{1}} - \underline{n}\otimes\underline{n} \tag{15}$$

On the other hand in case of a segregated code the BC is only partially implicit as can be seen from the following example for the mesh velocity BC in the vertical direction

$$A_3 = -n_3 n_1 w^n_{I,1} - n_3 n_2 w^n_{I,2} \text{ and } B_3 = 1 - n_3^2 \tag{16}$$

Convective outlet In order to avoid pressure perturbation being reflected from the outlet back into the domain a convective boundary condition has been implemented. The general formulation reads:

$$\frac{\partial\phi}{\partial t} + U\frac{\partial\phi}{\partial n} = 0 \tag{17}$$

with ϕ a generic variable that has to be convected out of the domain and *where U is a velocity that is independent of the location on the outflow surface and should be chosen in order to satisfy the overall balance of mass.* Using a first order discretization for both the temporal and the convective term Eq. (17) leads to:

$$\frac{\phi_F^{n+1}-\phi_F^n}{\Delta t} + U\frac{\phi_F^{n+1}-\phi_{I'}^{n+1}}{\overline{I'F}} = 0 \tag{18}$$

where I denotes cell centre of mass, F for the face centre and $\overline{I'F}$ the distance between I and F. Introducing the Courant number defined as $CFL = U\Delta t/\overline{I'F}$ Eq. (18) can be rearranged as:

$$\phi_F^{n+1} = \underbrace{\frac{1}{1+CLF}\phi_F^n}_{A} + \underbrace{\frac{CFL}{1+CLF}}_{B}\phi_I^{n+1} \tag{19}$$

An alternative formulation is possible usin a θ scheme for the time discretisation of the convective term. This reads:

$$\frac{\phi_F^{n+1}-\phi_F^n}{\Delta t} + U\frac{\phi_F^{n+\theta}-\phi_{I'}^{n+\theta}}{\overline{I'F}} = 0 \tag{20}$$

where $\phi^{n+\theta} = \theta\phi^{n+1} + (1-\theta)\,\phi^n$ and after some rearrangements the value at the face centre takes the following formulation:

$\rho\ \left[kg/m^3\right]$	$g\ \left[m/s^2\right]$	$\mu\ [kg/m/s]$	$d\ [m]$	$A\ [m]$	$c\ [m/s]$
10^3	10	10^{-12}	1	$0.2d$	3.46

Table 2: Definition of the physical and wave parameters for the solitary wave test case.

$$\phi_F^{n+1} = \underbrace{\frac{1 - CFL\,(1-\theta)}{1+\theta CFL}\phi_F^n + \frac{CFL\,(1-\theta)}{1+\theta CFL}\phi_I^n}_{A} + \underbrace{\frac{\theta CFL}{1+\theta CFL}}_{B}\phi_I^{n+1} \tag{21}$$

It is important to note that in case of $\theta = 1$ (i.e. first order in time) the formulation of Eq. (18) is recovered, whereas in case of $\theta = 0.5$ a second order in time is achieved.

Both Eqs. (19) and (21) follow the decomposition of Eq. (10) and therefore the coefficient B can be made implicit. A second possibility is also to directly impose a Dirichlet condition, always using Eq. (19), but keeping in mind that this definition is totally explicit[1]. The effect of using a pure Dirichlet or a partially implicit boundary condition is investigated in Sec. 2.3.1.

2.3 Test cases

In this section three test case are presented in order to validate the ALE and free-surface modules. A comparison between V_2.0 and V_2.2 of *Code_Saturne* is also presented.

2.3.1 Solitary wave

The solitary wave is a typical test case for free-surface validation. It has been introduced by Russell (1844) with the following analytical definition for the free-surface elevation:

$$\eta(x_1, t) = A\mathrm{sech}^2\left(k\left(x_1 - ct\right)\right) + d \tag{22}$$

with A the maximum wave height, the crest velocity $c = \sqrt{g_3\left(h + A\right)}$ and h the undisturbed water depth. Here, x_1 represents the stream-wise direction and x_3 is the vertical. The wave has an infinite wavelength, but by convection a wave number is defined as

$$k = \sqrt{\frac{3A}{4d^3}} \tag{23}$$

From here it is possible to define the following inlet boundary condition for the inlet velocities:

$$\begin{cases} u_1\left(x_{inlet}, t\right) = c\dfrac{\eta\left(x_{inlet}, t\right)}{d + \eta\left(x_{inlet}, t\right)} \\ \dfrac{\partial u_3}{\partial x_3}\left(x_{inlet}, t\right) = 2khu_1\left(x_{inlet}, t\right)\dfrac{\tanh\left(k\left(x_1 - ct\right)\right)}{d + \eta\left(x_{inlet}, t\right)} \Rightarrow u_3 = \dfrac{\partial u_3}{\partial x_3}\cdot x_3\left(t\right) \end{cases} \tag{24}$$

The computational domain has the following dimension $10\pi \times 0.1 \times 1$ in the stream wise, span-wise and vertical directions respectively using the following resolution $500 \times 1 \times 20$. Calculations are performed in the inviscid limit (i.e. $\mu \to 0 \Rightarrow Re \to \infty$) and with a maximum amplitude $A = 0.2h$. Tab. 2 gives a summary of the physical and wave parameters employed.

As already mentioned the inlet definition of the velocity components is given in Eq. (24), whereas the outlet follows Eq. (18) where the convective speed $U = c$. At the free surface all variables are assigned a homogeneous Neumann condition with the exception of the pressure, for which fixed value is imposed equal to the reference pressure. For all remaining boundary faces a slip condition is imposed. In the case of the mesh velocity a fixed mesh is imposed at the bottom, whereas all the side faces have got a sliding condition.

[1] In case of a pure Dirichlet condition for the pressure one has to remember to include also the reference and the piezometric pressure.

Figure 2 presents the free surface elevation at six different time steps. In all the simulations the wave propagation is relatively well predicted. A very small exception is a lag of the wave displacement with respect to the theory, which is present in all simulations, but it is more evident in V_2.0 cases. As the simulation time progresses, V_2.2 tends to slightly damp the maximum amplitude A, whereas V_2.0 tends to do the opposite. With the propagation of the wave (see time $= 12\,s$) the prediction of the tail of the wave becomes less accurate, with the tendency to form a small trough behind the soliton. After the passage of the wave the free surface does not return to an unperturbed state, but small oscillations are present. Larger oscillations are also present at the inlet during the descending phase of the wave. This phenomenon is present in all simulations with waves, but it does not seem to affect the stability of the simulations. The last consideration that has to be made is about the influence of the formulation of the convective outlet. In this test only the first order in time discretisation has been used (see Eq. (19)). The fix Dirichlet conditions produces a very large pressure reflection (see Figure 3), which generates a partial reflection of the wave. The same phenomenon occurs also in the partially implicit method used to impose the BC at the outlet, but the reflection is negligible. Figure 4 shows the time evolution of the CPU time for all simulations. On average V_2.2 is 40% faster than V_2.0 and this can be easily explained with the fact that the ALE procedure in V_2.0 requires several free surface loops in order to satisfy the kinematic boundary condition, looping that is not necessary in the new version. Despite the iterative procedure the mass flux through the free surface in V_2.0 is of the order of 10^{-7}, whereas in V_2.2 it is of the order of the machine precision (i.e. $\sim 10^{-17}$).

2.3.2 Regular Waves

A second common test case for validation of ALE methods is the propagation of water waves with a uniform current. The velocity potential has to represent both a progressive wave and a uniform current with velocity U_0 and satisfy the Laplace equation. A possible formulation reads:

$$\phi = -U_0 x_1 + A \frac{g}{\omega \left(1 - \dfrac{U_0}{c}\right)} \frac{\cosh\left(k x_3\right)}{\cosh\left(k d\right)} \cos\left(k x_1 - \omega t\right) \tag{25}$$

where ω is the angular frequency, k the wave number, A the peak amplitude, d the water depth, $c = \omega/k$ the celerity. As in Sec. 2.3.1 x_1 is the stream wise direction, whereas x_3 is the perpendicular one. The form of the potential given by Eq. (25) guarantees that the solution is periodic in time and space, satisfy the no-flow bottom boundary condition and the dynamic free surface boundary condition (DFSBC), where the free surface elevation has the following formulation:

$$\eta\left(x_1, t\right) = A \sin\left(k x_1 - \omega t\right) + d \tag{26}$$

The last boundary condition that needs to be satisfied is the linear form of kinematic free surface boundary condition (KFSBC), which yields the following dispersion relation[2]:

$$\left(\omega - k U_0\right)^2 = g k \tanh\left(k d\right) \tag{27}$$

where the term kU_o represents a Doppler shift. Finally from Eq. (25) it is possible to get the definition for the particle velocity as:

[2]In this work it is assumed that the direction of the propagation of the wave and direction of the current are the same (i.e. the angle between $\underline{U_0}$ and the x_1 is equal to 0). The more general form of the dispersion relation reads:

$$\left(\omega - \underline{k} \cdot \underline{U_0}\right)^2 = g k \tanh\left(k h\right)$$

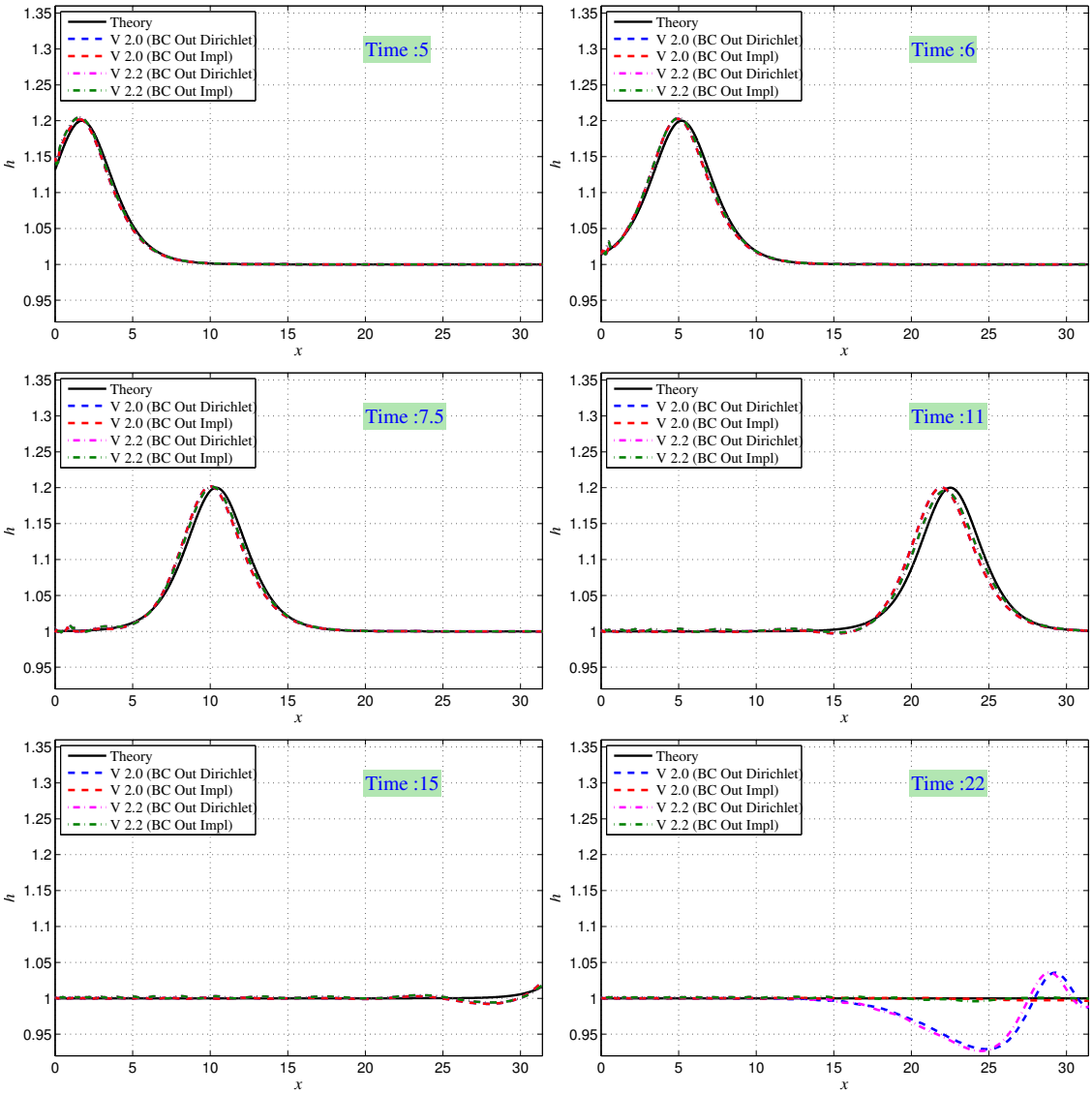

Figure 2: Free surface elevation for the solitary wave for different versions of *Code_Saturne* and different implementation of the convective outlet.

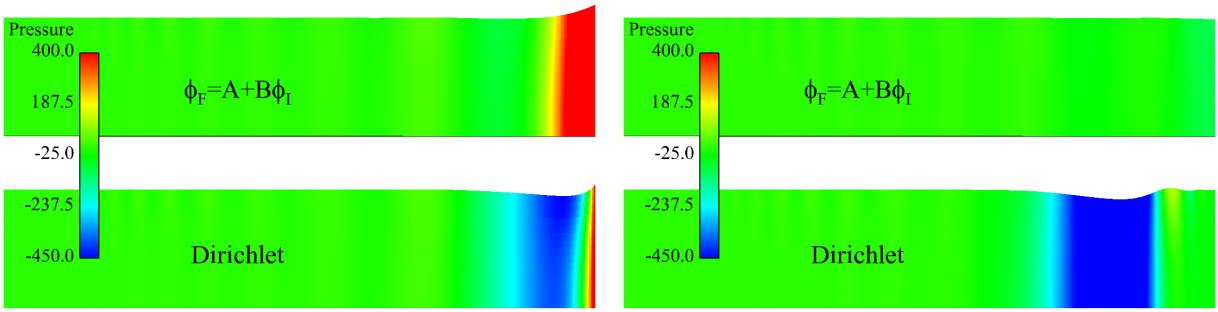

Figure 3: Comparison of pressure field $p = p_{TOT} - p_0 - \rho g\,(z - d)$ at time $= 15\,s$ (left) and at time $= 22\,s$ (right).

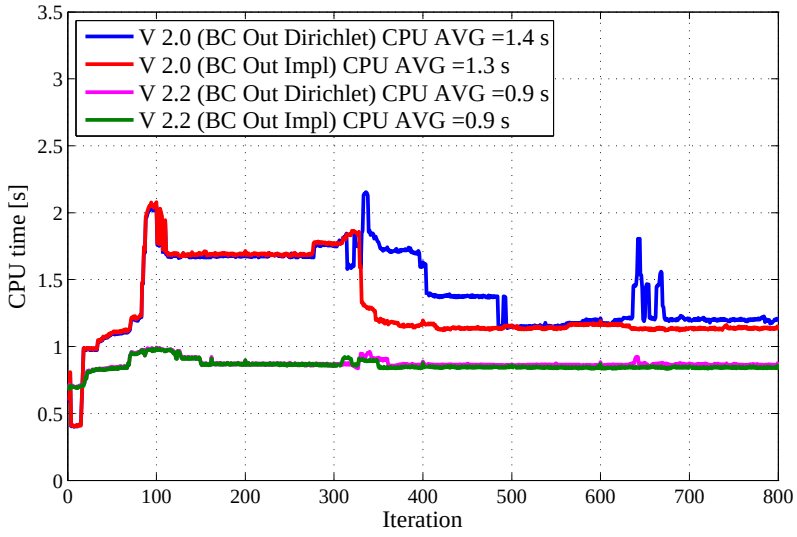

Figure 4: CPU time as function of the iteration number for different versions of *Code_Saturne* and different implementation of the convective outlet.V_2.0 results are obtained with FS loop.

$$\begin{cases} u_1 = -\dfrac{\partial \phi}{\partial x_1} = U_0 + A \dfrac{gk}{\omega\left(1 - \dfrac{U_0}{c}\right)} \dfrac{\cosh(kx_3)}{\cosh(kd)} \sin(kx_1 - \omega t) \\ u_3 = -\dfrac{\partial \phi}{\partial x_3} = A \dfrac{gk}{\omega\left(1 - \dfrac{U_0}{c}\right)} \dfrac{\sinh(kx_3)}{\cosh(kd)} \cos(kx_1 - \omega t) \end{cases} \tag{28}$$

It is possible to relate the solution obtained above in a stationary system of reference to a moving one with a velocity U_0. In both the systems the wave length is the same and two periods are related as:

$$T = T'\left(1 - \frac{U_0}{c}\right) \tag{29}$$

where $T = 2\pi/\omega$ is the period in the absolute system and $T' = 2\pi/\omega'$ the period in the relative system. Therefore the total particle velocity can be decomposed in two contributions $\underline{U_0} + \underline{u_w}$, where $\underline{u_w}$ is the wave contribution[3]. For the specific case of $U_0 = 0$ the usual relations for progressive waves are recovered. For more details about wave theory the reader should refers to Dean and Dalrymple (1991).

Two different regular waves are simulated with parameters reported in Table 3. The first wave is the same that has been simulated by Yacine Addad for free surface validation using *Code_Saturne* V_1.3. The second is more similar to the wave conditions considered in the simulation of the TGL marine turbine in Sec. 5.3. For Wave1 two different resolutions have been employed (500×20 and 1000×40) and only V_2.2 is tested. For Wave2 only one resolution has been used (500×42) and the case will be used to benchmark the different versions of the ALE module. All simulations are performed in the inviscid limit (i.e. $\nu \to 0$)

[3]The wave contribution can be computed in the relative system, but one has to be carefully since the term $\dfrac{gk}{\omega\left(1 - \dfrac{U_0}{c}\right)} = \dfrac{gk}{\omega'}$, but the argument of the trigonometric function still has a ω (i.e. $\cos(kx_1 - \omega t) \neq \cos(kx_1 - \omega' t)$).

	Wave 1	Wave 2		Wave 1	Wave 2
Water depth d	1	45	Angular frequency ω	0.785	0.698
Amplitude A	5% of d	4% of d	Wave number k	0.88	0.05
Stream-wise domain length L_x	10π	660	Wave length λ	7.17	123.8
Wave period T	8	9	kd	0.88	2.25
Gravity g	10	9.81	Celerity c	0.9	13.76

Table 3: Normalised flow parameters for the regular wave simulation

Fig. 5 plots the free surface elevation at six different time steps. After an initial evolution where the free surface presents some oscillatory behaviour at peaks and troughs, the wave propagation match with a very good agreement the theoretical behaviour. A problem arises in the solution after some time: the wave propagation is still correct, but the free surface elevation reduces or in other words there is a net mass loss from the outlet. This problem is illustrated by the plot of the time history of the maximum and minimum pressure in the domain (see Fig. 6): until $100\,s$ values are roughly constant, but after they start both to decrease with the same negative slope. It is interesting to notice that the increase of mesh resolution does not have any influence on the phenomenon for the same time step in both simulations. On the contrary, the reduction of CFL number has the beneficial effect to delay the problem to later time as clear from Fig. 7: indeed delay, but not completely remove.

Two possible solutions have been devised in order to alleviate the problem. The first is the modification of the pressure at inlet and outlet in order to conserve the total mass. This correction (BCP) has to be opposite on the two faces and reads

$$p_{inlet} = p - \frac{c\Delta t}{L_x}\rho g\Delta \quad p_{outlet} = p + \frac{c\Delta t}{L_x}\rho g\Delta \tag{30}$$

The second possibility is to introduce a source term in the momentum in the stream wise direction (QDM) and is defined as:

$$\frac{dp}{dx} = -\rho g\frac{\Delta}{l} \tag{31}$$

Δ is an error and can evaluated in different ways and l a reference length-scale. The first is to consider the instantaneous free surface elevation h at the inlet (ERRH) obtaining:

$$\Delta = h_{theory}\left(t\right) - h\left(t\right) \tag{32}$$

where $h_{theory}\left(t\right)$ is given by Eq. (26). A second possibility is to base the error estimation on the average water depth (ERRD) resulting in:

$$\Delta = d - \langle d\rangle^n \tag{33}$$

where d_{avg} is the average water depth that can be evaluated at the inlet and the average procedure can be performed using a running average of a specify time window [4] aT

$$\langle d\rangle^n = \frac{\Delta t}{aT}h^n + \left(1 - \frac{\Delta t}{aT}\right)\langle d\rangle^{n-1}$$

In case of the error definition based on instantaneous water depth (ERRH) the reference length $l = L_x$, whereas for ERRD $l = d$.

Figs. 8 and 9 show the time history of the max and min pressure and the free surface elevation at time 600 for the highest CFL number. With respect to the simulation of Fig. 7 it is obvious the downward shift is cancelled and the wave is still propagating properly.

[4] In these calculations the typical time window is equal to $5T$.

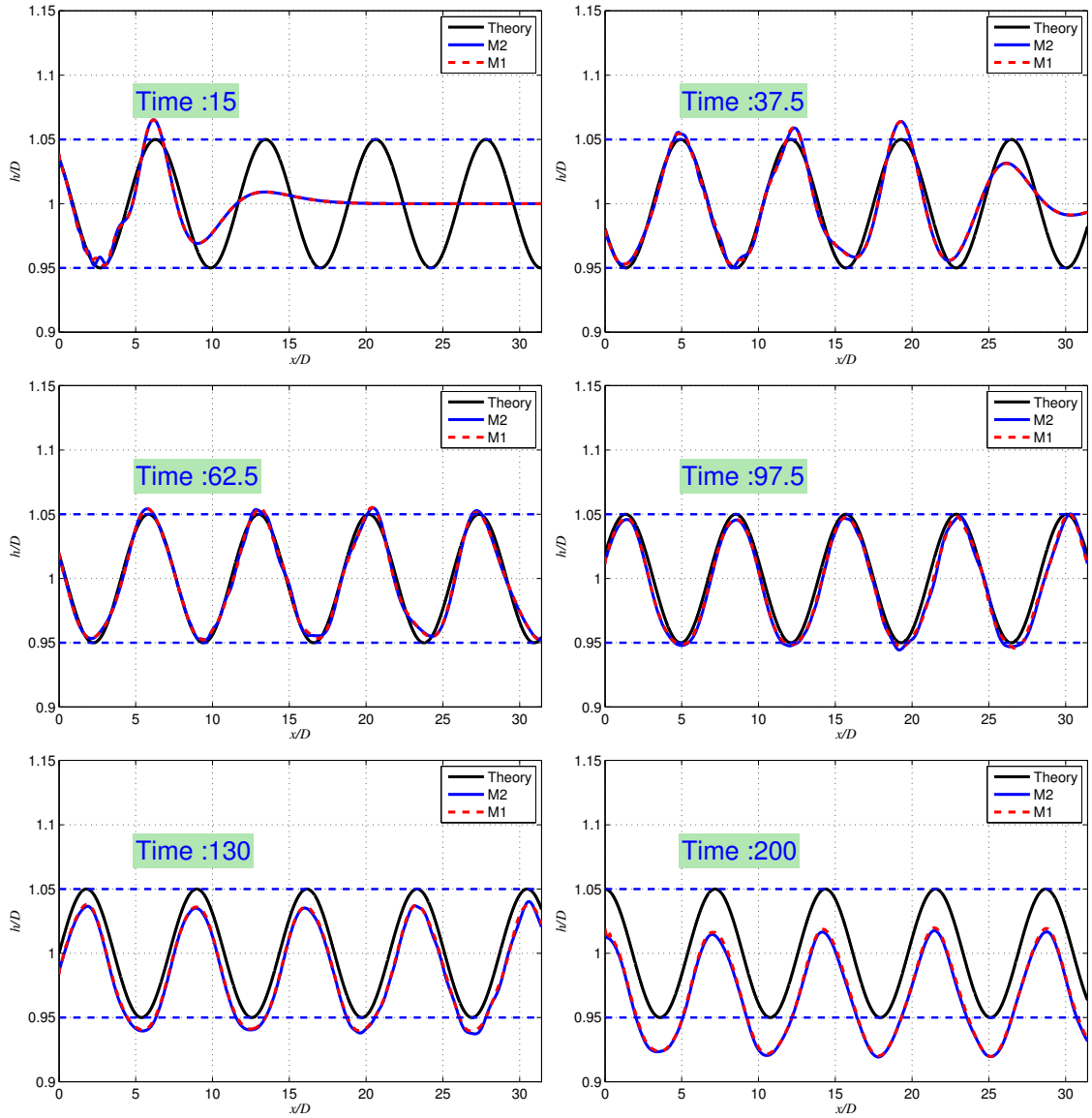

Figure 5: Free surface elevation for the regular wave for two mesh resolutions at six different time steps. Domain dimensions: $10\pi \times 1$, $T = 8\,s$, $g = 10\,m/s^2$. M1: 500×20, M2: 1000×40

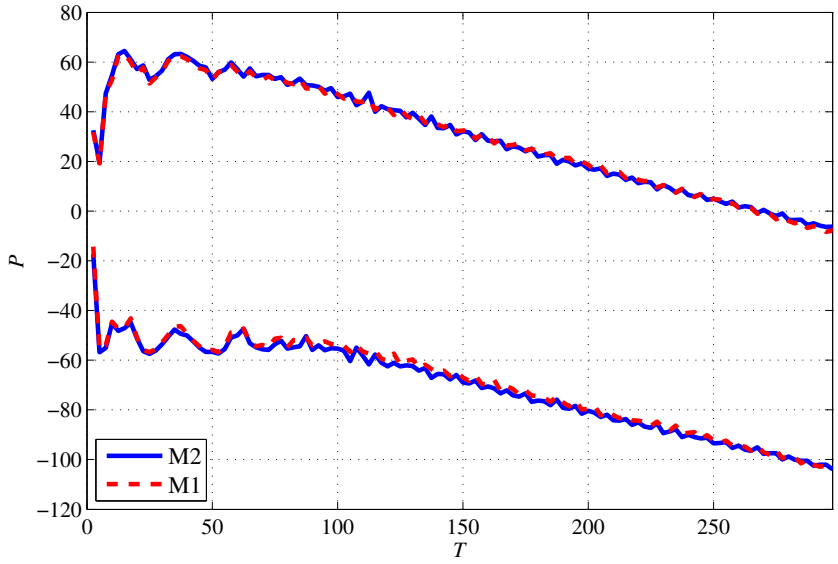

Figure 6: Time evolution of the maximum and minimum pressure for a regular wave. Domain dimensions: $10\pi \times 1$, $T = 8\,s$, $g = 10\,m/s^2$. M1: 500×20, M2: 1000×40

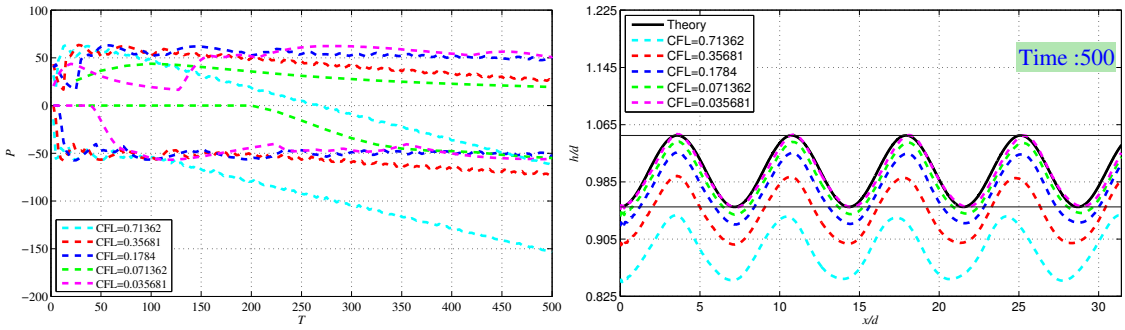

Figure 7: Time evolution of the maximum and minimum pressure for a regular wave (left) and surface elevation (right) for different values of the $CFL = c\Delta t/\Delta x$ number . Domain dimensions: $10\pi \times 1$ with M1: 500×20, $T = 8\,s$, $g = 10\,m/s^2$.

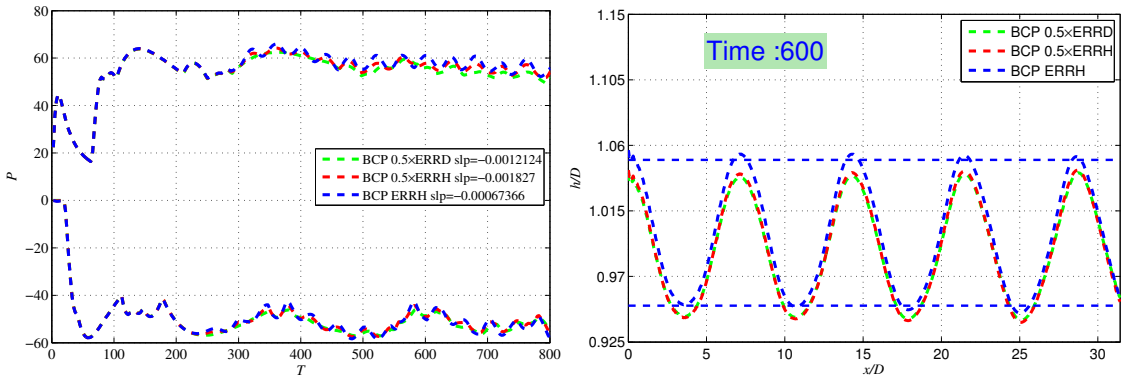

Figure 8: Time evolution of the maximum and minimum pressure for a regular wave (left) and surface elevation (right) for BCP correction at $CFL = 0.71$. Domain dimensions: $10\pi \times 1$ with M1: 500×20, $T = 8\,s$, $g = 10\,m/s^2$.

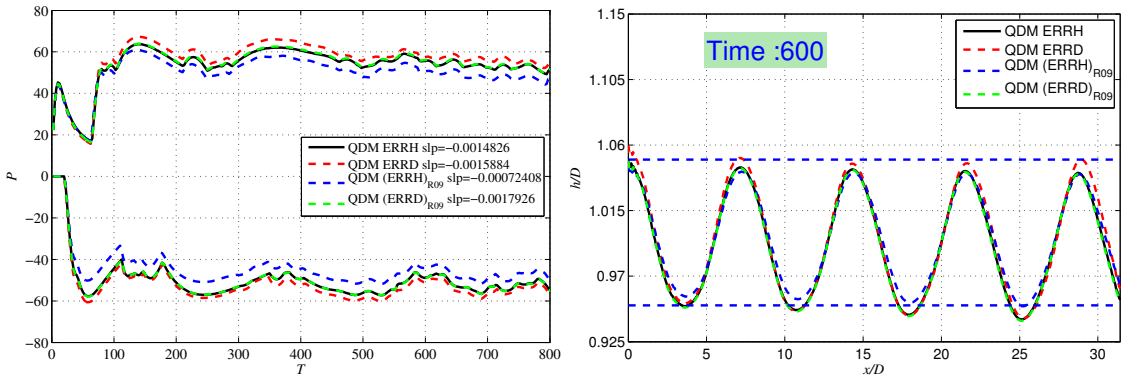

Figure 9: Time evolution of the maximum and minimum pressure for a regular wave (left) and surface elevation (right) for QDM correction at $CFL = 0.71$. Domain dimensions: $10\pi \times 1$ with M1: 500×20, $T = 8\,s$, $g = 10\,m/s^2$.

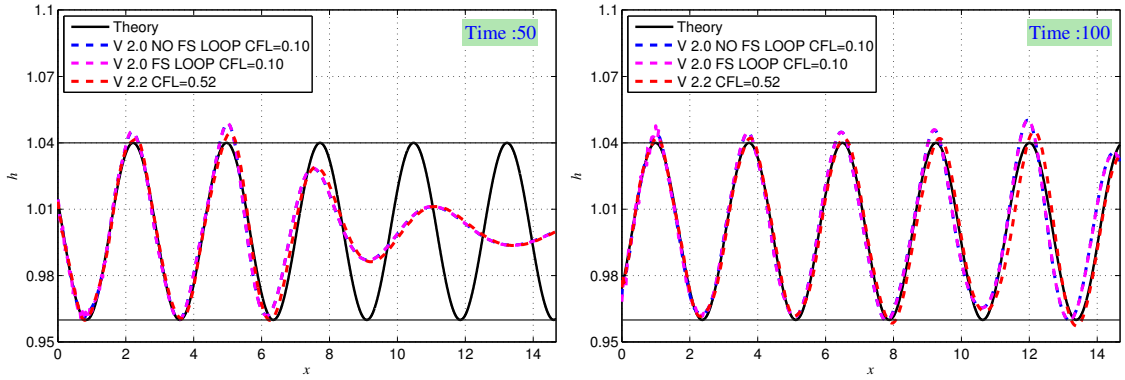

Figure 10: Free surface elevation for the regular wave for two mesh resolutions at two different time steps. Domain dimensions: 660×43, $T = 9\,s$, $g = 9.81\,m/s^2$

In case of Wave2 Fig. 10 reports the free-surface elevation at two different time steps for different versions of the ALE module. Both methods seems to correct the mass loss, with the only exception of a small overestimation of peak values close to the outlet in both V_2.0 simulations. V_2.2 results are obtained with a larger time step showing the improved robustness of the new *Code_Saturne* release, which uses a coupled solver. This is not a major issue since in the real turbine calculation, time step is already constrained to relatively small values by the sliding mesh module.

2.4 Conclusions on the ALE module

The simulations of MD1.1 and MD1.2 were conducted using *Code_Saturne* version V_2.0. Since MD1.2 was completed a new version of *Code_Saturne* has been released (V_2.2) that includes a new ALE module for the free surface. The sliding mesh module has been verified in V_2.0 only and modifications are required to use this module in V_2.2. These changes would be time-consuming to implement and verify. Therefore, V_2.0 was chosen for the simulations of the turbine with waves in this report. To enable these simulations a new ALE module has been implemented under V_2.0 of *Code_Saturne*. This module uses some of the features of the V_2.2 ALE module (see Ferrand (2011)) to improve the speed-up performances with respect to the original formulation. This development was essential so that the ALE module does not limit the time-step used in the turbine simulations with waves. The modified ALE module for V_2.0 still exhibits some of the

drawbacks of the original V_2.0 ALE module (i.e. stability with large time steps). However, this module yields similar accuracy to V_2.2 and so this approach will be used for MD1.4 simulations. As such a possibly time-consuming process of verification of the V_2.2 implementation of the sliding mesh module will be avoided.

In all versions of the ALE free surface method, wiggles occur shortly downstream of the inlet. Both types of waves (solitary and regular) suffer from this phenomenon, but it did not affect the stability of the present simulations. However, this does limit the wave steepness that can be addressed. Further analysis is on-going to address this issue and enable simulation of steeper waves.

3 Parallel implementation of the sliding mesh

The sliding-mesh method is validated well against a rotating cylinder, sphere, cube and a TST (see MD1.2 for all validation cases). However, CPU time and scalability (see Table 4) have been raised as an issue that would limit the duration and the resolution of the Tidal Stream Turbine simulations. Therefore a new implementation of the method was necessary, in particular a better optimisation of the MPI (message passing interface) calls.

CPU Time per Iter	117.5 s
Group function	CPU time %
MPI	94.2
MPI_Allgatherv	67.4
MPI_Barrier	11.7
MPI_Allreduce	9.1
USER	4.9
gradmc	1.9
ETC	0.9

Table 4: Profiling of the Soton turbine using V2.8 of the sliding mesh module for an LES calculation on a 7.2M control volumes for 512 cores on HeCTOR machine.

CPU Time per Iter	25.8 s
Group function	CPU time %
MPI	68.6
MPI_Barrier	37.6
MPI_Allreduce	15.8
MPI_Wailall	5.6
USER	28.2
gradmc	1.04
ETC	3.2

Table 5: Profiling of the Soton turbine using V6.1 of the sliding mesh module for an LES calculation on a 7.2M control volumes for 512 cores on HeCTOR machine.

The sliding mesh method used in MD1.2 was version 2-8 in its development with its performance over multiple cores shown in Fig. 12. The graph shows the CPU time per iteration for several implementations (described below) for a 3million cell mesh on the University of Manchester Computational Shared Facility.

The first stage in improving performance is to re-implemented using modules and reordering some subroutines and MPI calls optimise the performance. V5-4 in Fig. 12 shows the improvement of scalability in this respect. To further improve performance modifications to the parallel calls are made. This is best described by the example of Fig. 11a where the left and right sides of a sliding-mesh interface are shown. The number in each cell represents the process number that the cell is on. For separate processes to communicate requires an MPI call to be made. In the example there are 8 processes numbered 0-7, although processes 6 and 7 are not part of the sliding-mesh interface.

The previous developments (V2-8 and V5-4) use the MPI_Allgatherv call, which sends and receives data between all processes as shown in Fig. 11b. By creating an additional MPI group this communication need only occur between processes involved on the sliding-mesh interface as in Fig 11c. The final result is an increase in performance as shown by V5-7 in Fig. 12.

As a further development it has been decided that processes on the left side need only communicate with the right, and vice-versa, because this is the only data they require. This reduces all communications even further as shown by Fig. 11d. This is not trivial, the MPI_Allgather function is a blocking call, which ensures all processes will send and receive safely before the program continues. To implement this method requires two non-blocking calls: MPI_Isend and MPI_Irecv as well as a wait function. This has been implemented as V6-2 with its performance clear again on the performance graph.

It is also noted processes need only talk to those immediately adjacent, for example process 0 only needs to send and receive data with process 4 and 5 in 11a. Whilst reducing the communication time significantly this also requires a method for identifying adjacent processes as well as a communication between all processes to indicate if they should communicate in future. This latter idea has not been taken yet into practice, but it might be considered in case of improving scalability on large parallel calculations.

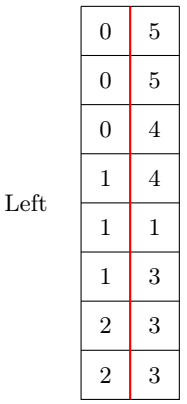

(a) Example of cells on interface split between six processes.

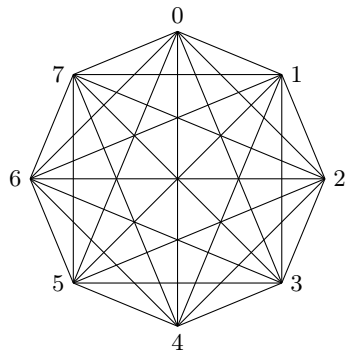

(b) Messages between all processes.

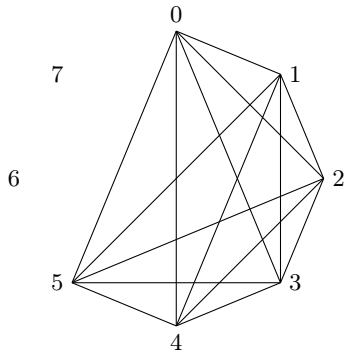

(c) Messages only between processes with elements on the interface.

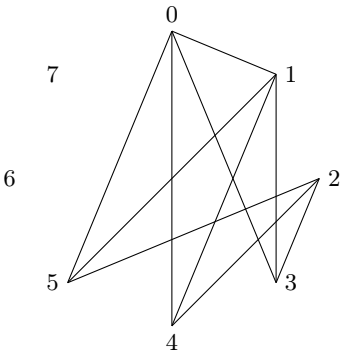

(d) Messages only between opposite side of the interface.

Figure 11: The result of MPI calls for compiling global arrays across four processes.

As shown by Fig. 12 and by comparing Table 4 with 5 subsequent developments have improved performances significantly and this is also confirmed by the scalability test performed on HeCTOR (see Fig. 13). As obvious this new implementation of the sliding mesh has been validated and results are similar to the one reported in the previous deliverable MD1.2. The project has applied and been granted time on HeCTOR to run the LES with waves calculations for MD1.4. However, the poor scalability of the original implementation meant the calculations would not have been allowed to run. This has now been made possible by the improvement of the code's performance. In comparison with a standard non-moving mesh calculation (T-Junction test case on Fig. 13) on similar mesh size is far more performant and additional work on the parallelisation of the method might be considered. On the other hand LES calculations will require addition of several control volumes in the outer domain in order to properly resolve the wake behind the turbine and the upstream region where the Synthetic Eddy Method will be applied. As a consequence the sliding interface will have a less important role in the parallel communications and scalability performances might improve.

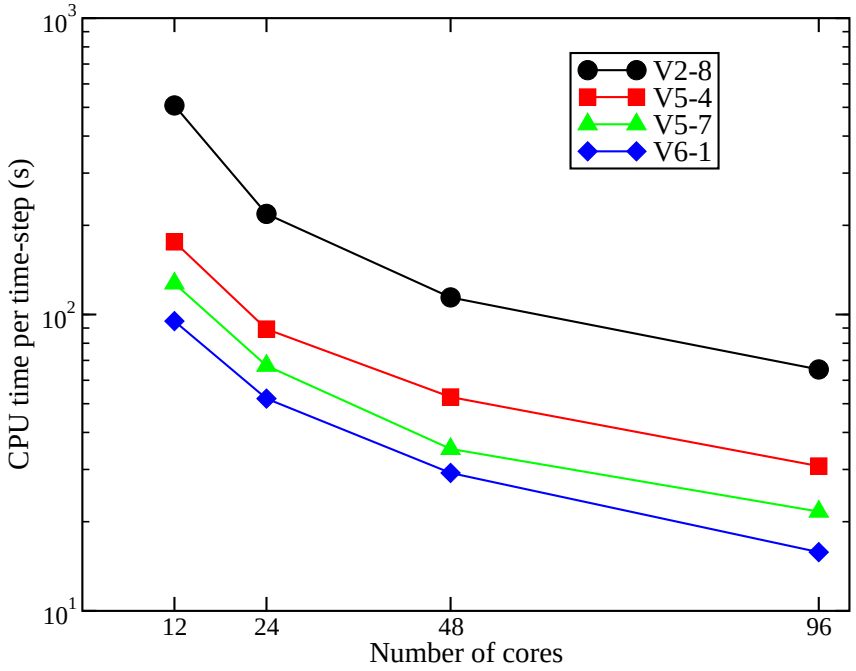

Figure 12: Speed-up for the sliding mesh method on the Computational Share Facility at University of Manchester.

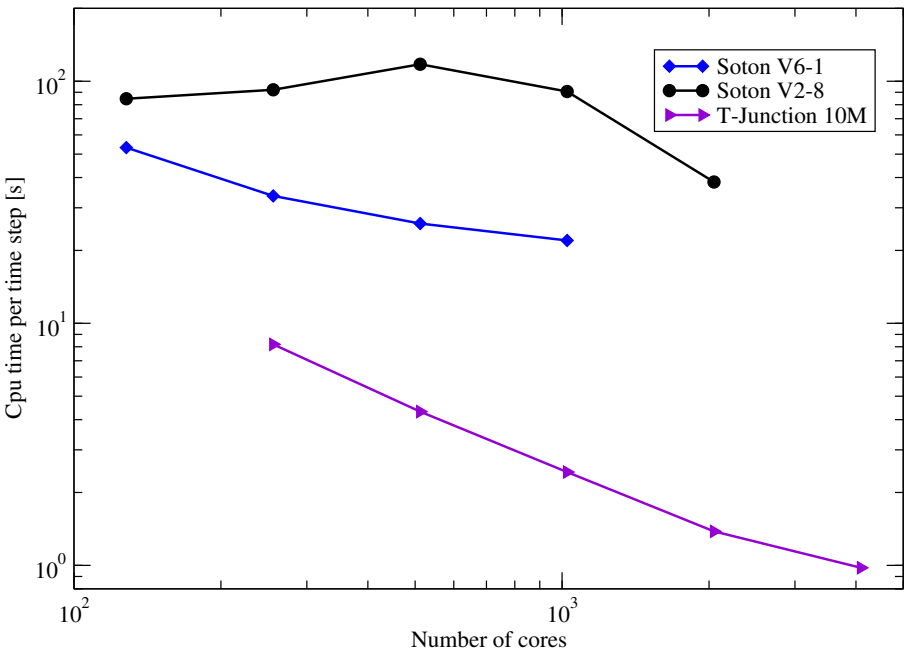

Figure 13: Speed-up for the sliding mesh method on HeCTOR and comparison with standard calculation.

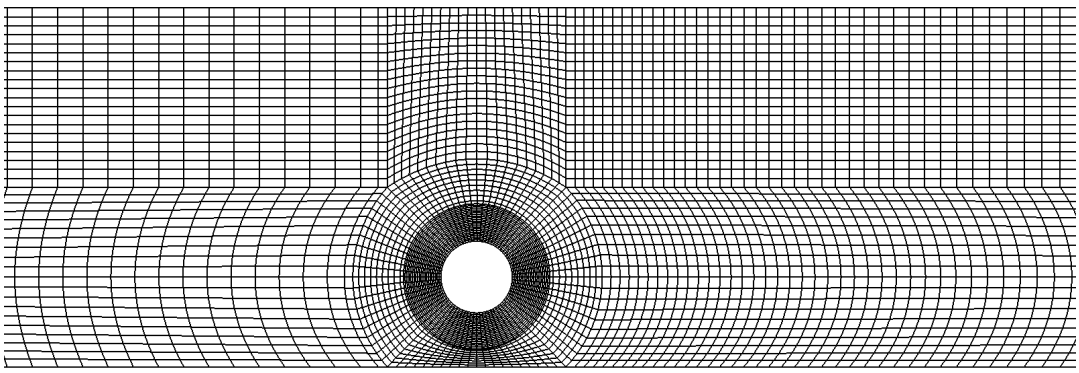

Figure 14: Zoom in the central region of the mesh used for the rotating cylinder

4 Regular wave passing over a rotating cylinder

In order to test the coupling between the sliding mesh module and the new ALE with free surface BC a simple test case of a regular wave passing over a rotating cylinder has been carried out both in 2D and 3D. Results are compared with the one obtained by Mittal and Kumar (2003) for a rotating cylinder at $Re = 200$ and $TSR = 1$. Indeed, in order to have a proper comparison the experimental data needs to be modified in order to take into account the hydrostatic contribution to the pressure. To evaluate this contribution we can start expressing the hydrostatic force acting on a infinitesimal surface with unit length in the span-wise as:

$$dF = -\rho g x_3 \mathbb{I} R d\theta \tag{34}$$

where $0 \leq \theta \leq 2\pi$ is the angle, R the cylinder radius and $\mathbb{I}$ the unit length in the span-wise direction. Of this force we are just interested on the component in the vertical direction x_3 and, indeed, we can express the vertical position in parametric form as function of the angle θ obtaining:

$$dF_{x_3} = -\rho g \mathbb{I} \left(x_{3_C} + R \sin\theta\right) R \sin\theta d\theta \tag{35}$$

Eq. (35) can be integrated between 0 and 2πobtaining as result $-\pi$. Therefore the hydrostatic force acting on a unitary length cylinder is:

$$F_{x_3} = -\rho g \mathbb{I} R^2 \pi \tag{36}$$

and therefore the following term has to be added to the lift coefficient[5] C_L:

$$\Delta C_L = -\frac{g\pi}{U_0^2} \tag{37}$$

The domain is constituted by a cylinder of radius $R = 1$ inside a rectangle (see Fig. 14). The position of the inlet is $23R$ upstream, the outlet $77D$ down-stream and the water depth is equal to $10R$. The centre of the cylinder is positioned $2.5R$ from the bottom surface and the interface between the rotor and the stator is at $3R$ from the cylinder centre. Inlet and outlet are discretised using 40 cells, whereas 150 are used for the top surface with a minimum spacing of $0.25R$ located over the top of the cylinder and a maximum of $1.65R$ located far in the wake for a total amount of control volumes equal to 8000. The 3D mesh is simply obtained with an extrusion in the span-wise direction of 10 cells for a total span length equal to R. The definition of the inlet is the same used in Sec. 2.3.2 for the regular wave test with a uniform current, symmetry is used on the front and back sides, a convective outlet at the exit and a no-slip wall at the bottom. Calculations

[5]It has to be noted that the gravity g is considered with sign

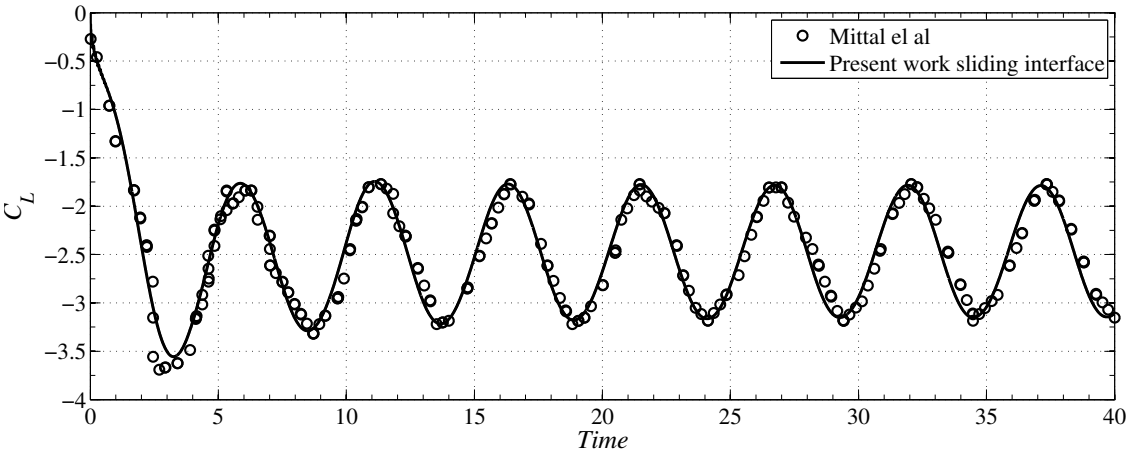

Figure 15: Time history of the lift coefficient C_L in the case of of a rotating cylinder in an unbounded domain and comparison with data from Mittal and Kumar (2003).

are performed using V_2.0 with the modified ALE module without any free surface loop (see Sec 2.2.1). In order to avoid the deformation of the rotating part of the mesh a limit on the mesh moment is imposed at a $5.5R$ from the bottom wall. Below this limit the mesh is fixed or it is rotating with a constant angular velocity.

4.1 Results

The case of a rotating cylinder at $Re = 200$ has been already used in MD1.2 for the validation of the sliding mesh method. As clear from Fig. 15 the agreement between the data obtained with the present method and the data from Mittal and Kumar (2003) is very good in both amplitude and period. Indeed the data from Mittal and Kumar (2003) consider a case of an unbounded cylinder inserted in a uniform current, therefore a direct comparison of lift coefficient between Mittal and Kumar (2003) and the case of a rotating submerged cylinder close to the ground is not very meaningful as the wake is largely altered by the interaction with the wall beneath (see Figs 18 until 17). In the literature there is a some work about rotating cylinders close to the ground (see for example Cheng et al. (2006)), but these works are again in the case of an unbounded domain on the top. In the unbounded domain the wake deviates toward the top, without and interaction with the top surface, which is located far away. On the other hand in the case considered herein there is as well an interaction between wake and free surface, which is located very close to the cylinder. As a consequence a direct comparison is not very relevant. Indeed the main objective of this section is to understand the difference between the case with a stress-free free-surface and waves and the influence of the wave parameters on the lift and drag coefficients. Three different simulations have been performed for both 2D and 3D mesh: the first with the free surface free to move, but no wave passing over the cylinder: the other two with instead a wave at a Froude number of 0.12 and 0.15 respectively. The Froude numbers ($Fr = U/c$) are obtained from a scaling $\sqrt{d_{TGL}/d_{CYL}}$ of the relative periods T', which are going to be used for the TGL simulations. Table 6 reports all the parameters used for the wave definition.

Figs. 16, 17 and 18 show pressure, velocity and mesh velocity at time $75\,s$ for the free-surface alone, $Fr = 0.15$ and $Fr = 0.12$ respectively. Flow features are relatively similar in both 2D and 3D, therefore only cut plane in the middle of the 3D geometry is reported. The first point that can be made is that the vortex shedding from the cylinder is still very clear in all three cases, but under the presence of a wave the shedding is interacting with the free surface with the results of a destruction of the very clear Von Kárman street of the no-wave case. This can be ascribed as the effect of pressure waves generated by peaks and troughs of the waves periodically hitting the cylinder. The other important flow feature to underline is the close interaction between the

	Wave1	Wave2
Water depth d	$10R$	$10R$
Amplitude A	3% of d	3% of d
Inlet Velocity U	1	1
Relative Period T'	5	3.5
Absolute period T	4.4	2.96
Celerity c	8.33	6.67
Froude Fr	0.12	0.15
Wave length λ	37.17	19.44

Table 6: Wave parameters definition for the regular wave over a rotating cylinder.

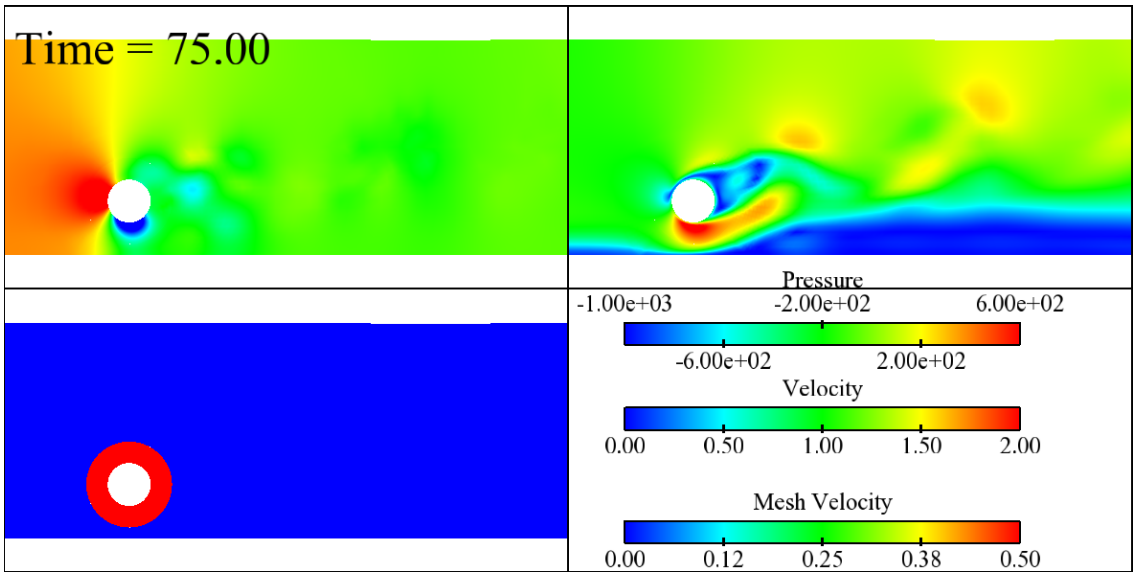

Figure 16: Pressure (top left), velocity module (top right) and mesh velocity module (bottom left) for the free surface only at time 75 s.

cylinder wave and the boundary layer generated by the bottom wall. The anti-clockwise rotation of the cylinder shrinks the boundary layer thickness just below the cylinder, boundary layer that rapidly grows and tends to push upward the wake. The last point that can be made is about the mesh velocity $\underline{w}$. In the no-wave case the mesh velocity outside the rotating sub-domain (red in the figure) is very small and, as a consequence, the maximum free surface displacement is below 5‰.

Figs. 20 and 21 report the lift and drag coefficients for all the cases. With respect to usual way to report the lift coefficient (see Fig 15) C_L is shifted up by a factor given Eq. 37, in order to take into account hydrostatic contribution to the pressure. Lift coefficient for the no-wave case shows a periodic and regular behaviour, but the Strouhal number for the case is equal to 0.27 instead of the usual $0.21 - 0.22$ reported for unbounded cylinders in the literature. The explanation for this difference might be searched in the interaction between the wake and the bottom boundary layer as explained above. In the wave passing-over cases C_L profiles are no more sinusoidal but exhibit an alternating behaviour with a high peak followed by a smaller, with a peak-to-peak amplitude larger in the $Fr = 15$ (i.e. smaller period) with respect to the other case. On the other hand in the case of the drag coefficient C_D all profiles are almost sinusoidal. This example demonstrates that the code developments enable simulations with both a free surface represented by the ALE algorithm and a rotating bluff body represented by the sliding mesh method.

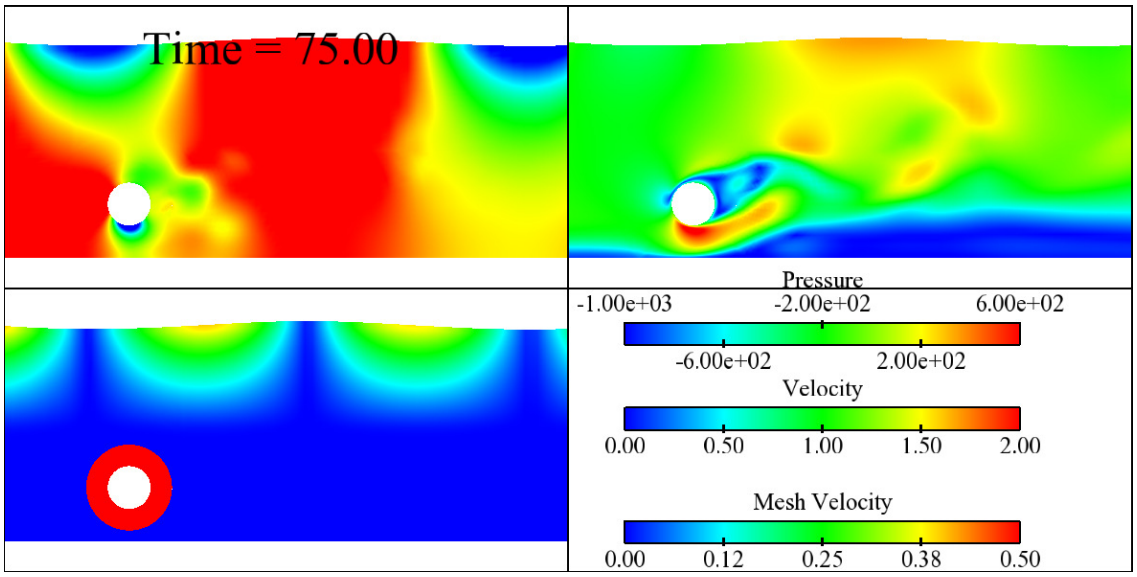

Figure 17: Pressure (top left), velocity module (top right) and mesh velocity module (bottom left) for the $Fr = 0.15$ at time $75\,s$.

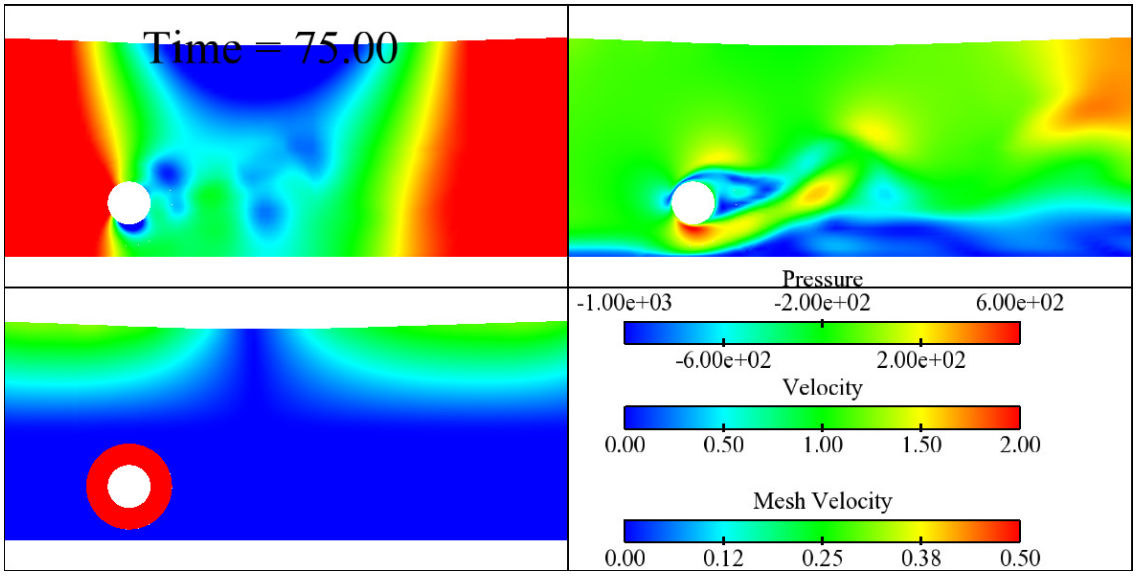

Figure 18: Pressure (top left), velocity module (top right) and mesh velocity module (bottom left) for $Fr = 0.12$ at time $75\,s$.

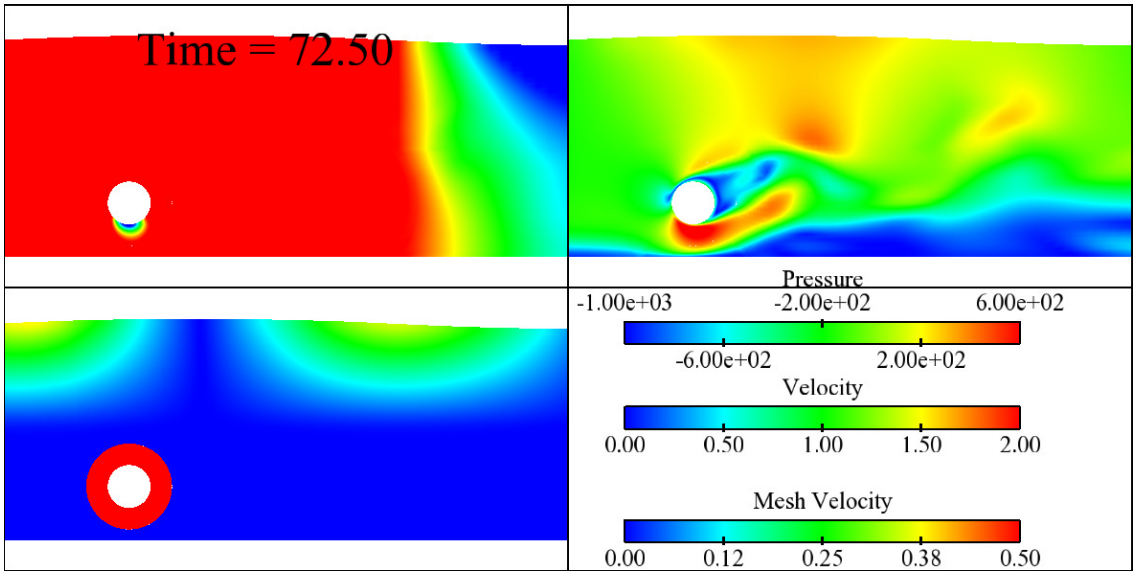

Figure 19: Pressure (top left), velocity module (top right) and mesh velocity module (bottom left) for the $Fr = 0.12$ at time 72.5 s.

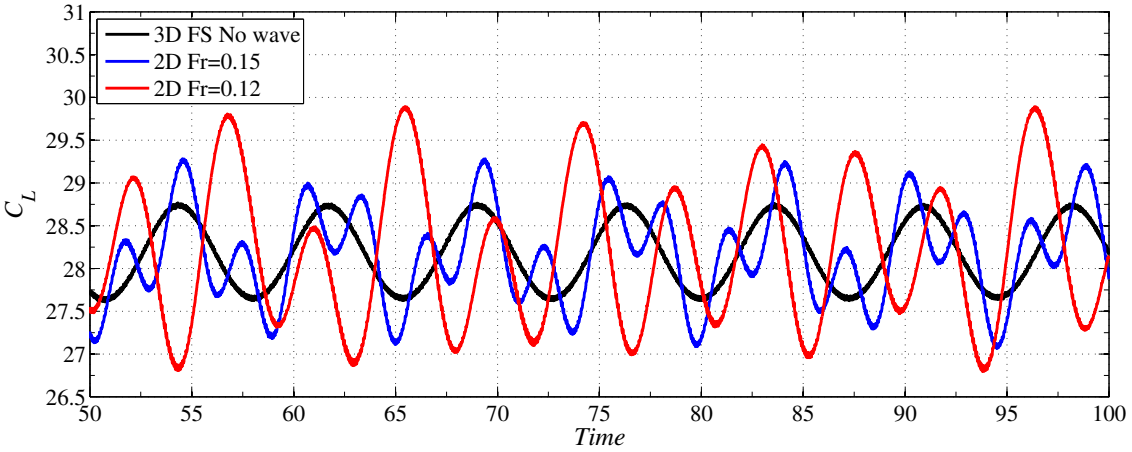

Figure 20: Time history of the lift coefficient C_L.

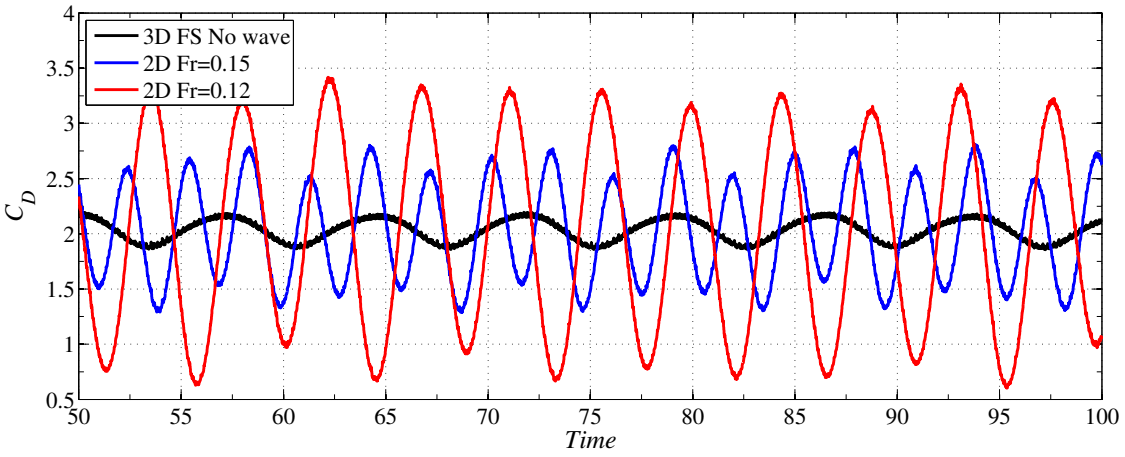

Figure 21: Time history of the drag coefficient C_D.

5 TGL Geometry

The modelled turbine is the 18m diameter (D) TGL 1MW turbine. The rotor, hub and nacelle geometry has been suppled by TGL to UoM in .step format (M-101494_1MW_turbine_110826.stp) as part of the project. For the simulation work reported here, the blades have been set to a pitch angle of zero as defined by TGL and a tip-speed ratio of 6 is imposed. Initial simulations are conducted with a uniform flow of 1.5 m/s.

5.1 Turbine Geometry definition

As with the Southampton turbine used in MD1.1 and MD1.2 the 1MW turbine blade is contracted in a 120^o segment, which can be copied twice around the axis of rotation. Ansys ICEM-CFD is used to create a block-structured grid. A blocking region is constructed to act as a guide for cells close to the blade as in Fig. 22a. The completed surface mesh is shown in Fig. 22b where the high cell-concentration towards the tip as well as leading and trailing edges is observed.

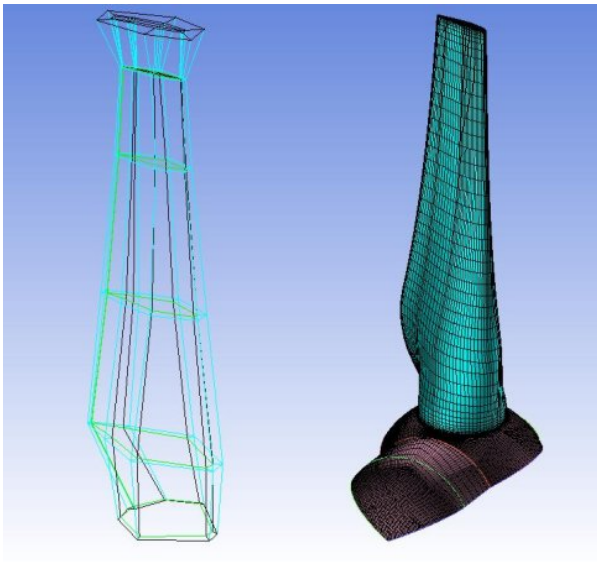

(a) Blade blocking (b) Surface blade mesh

Figure 22: TGL blade

An O-mesh is used around the blades. The choice of O-mesh is to handle the complex geometry of the blade's trailing edge, which is circular at the root and blends quickly to a sharp-edged hydrofoil along the length. Quality is maintained by the near-blade blocking (Fig. 23). For the simulations wall-functions are used to model flow close to the blades and the current mesh gives $y^+ < 300$ over the blades. At the tip the hydrofoil surface is split at one third from the trailing edge and further divided using nested O-meshes, shown in Fig. 24. This allows the cell count to be controlled at the tip without affecting the number of cells at the trailing edge. The large angle between the blade and the rotation plane at the root is shown in Fig. 25. To maintain a high-quality mesh block-structured mesh the meshes at the sides of the one-third section should align when duplicated. This creates issues of cell skewing and so control points are used on some edges to guide the mesh Fig. 26.

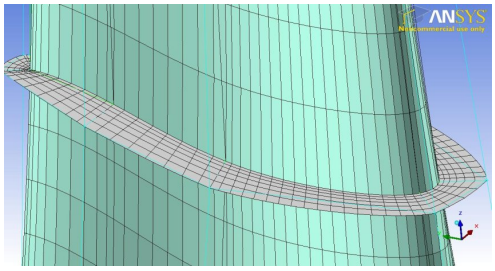

Figure 23: O-type mesh around the blade

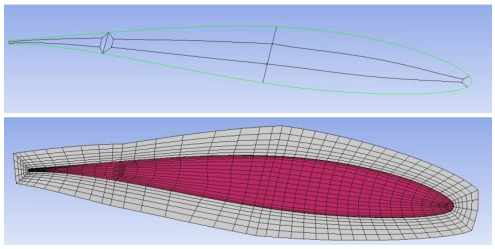

Figure 24: Mesh around the blade tip.

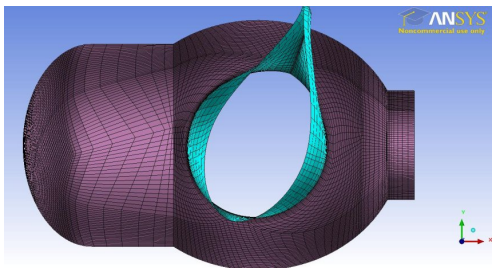

Figure 25: Blade twist

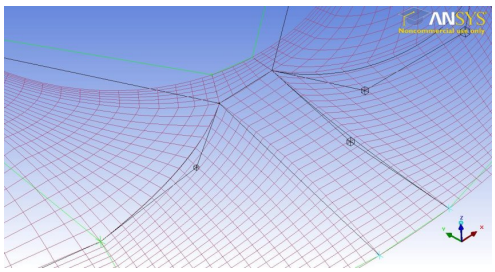

Figure 26: Blocking and mesh around the blade hub.

5.1.1 Domain

The domain is constructed in one section measuring $5D$ up-stream and $10D$ in the wake. The depth is 43 m ($2.4D$) with the turbine hub-height at 19.5m from the bed. The channel extends to $\pm 5D$ in the lateral direction which gives a blockage ratio of $\approx 3\%$. The complete outer domain is shown in Fig. 27a. Careful attention is given to ensuring orthogonal cells in the top most region to aid free-surface movement.

The nacelle (see Fig. 27b) is modelled based on the major dimensions of the 1MW device. Small protuberances and ancillary equipment on the outer surface of the nacelle are not modelled. A block-structured mesh is straightforward to fit over the surface, however, care is required to merge this with the mast and interface. Fig. 27c shows the complicated blocking structure required to maintain a high quality mesh around the nacelle and mast region.

5.1.2 Quality

The MD1.1 and MD1.2 simulations demonstrated that the solution stability is sensitive to cell skewness. This is measured by equiangle skewness:

$$\text{Equiangle sqew} = 1 - \max\left(\frac{\theta_{\max} - \theta_e}{180 - \theta_e}, \frac{\theta_e - \theta_{\min}}{\theta_e}\right),$$

with $\theta_{\max}$ and $\theta_{\min}$ the maximum and minimum angle in the face respectively and θ_e the angle of an equiangular face, for quadrilaterals (as in this case) 90^0. Analysis with CS has shown that meshes with a large number of cells under 0.4 in this quality criteria lead to poor results. A histogram showing the percentage of cells in each quality region is shown in Fig. 28 for both turbine and domain meshes. The quality is good for such a complex geometry with only a few elements less than 0.5 in both cases. The final results is a mesh with a size of $4.2 \cdot 10^6$ control volumes.

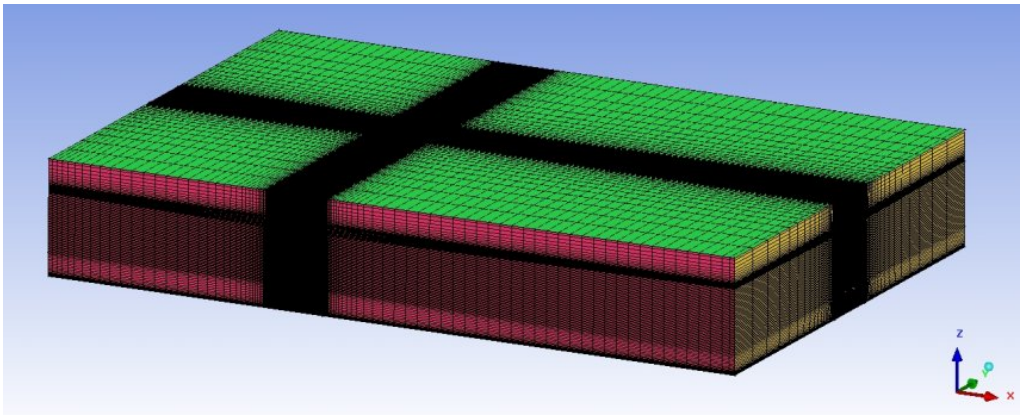

(a) External mesh

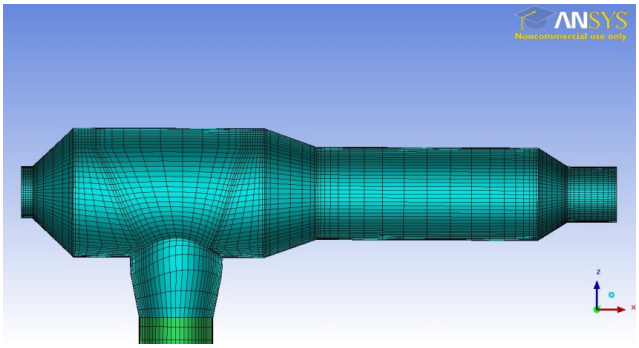

(b) External mesh

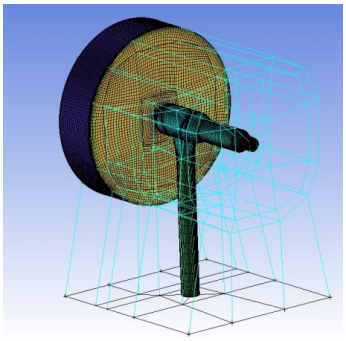

(c) External mesh

Figure 27: External domain

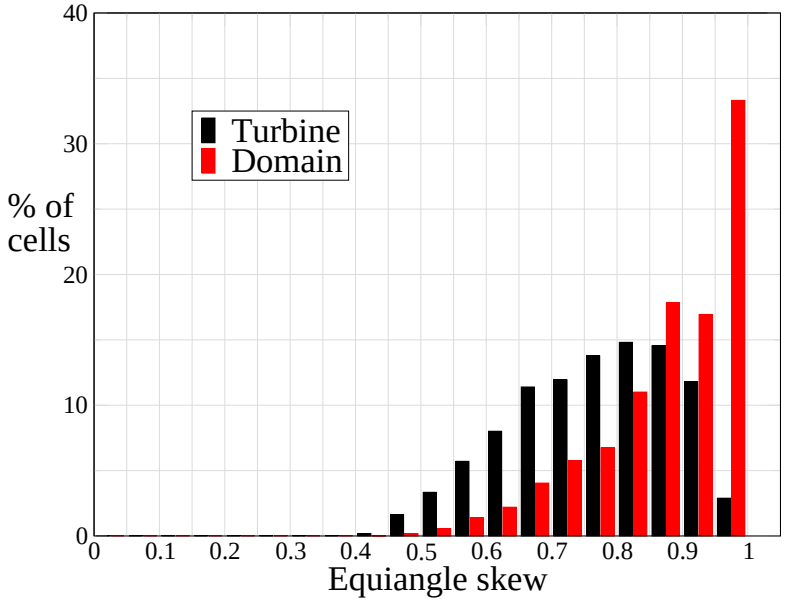

Figure 28: Histogram of equiangle skewness quality for turbine and domain meshes.

5.2 Simulations

5.2.1 Boundary conditions

The sides of the channel are given zero-flux slip symmetry conditions. The bed, and turbine (blades, nacelle, mast) are no-slip walls. Dirichlet conditions are specified at the inflow for the velocity and turbulent scalars. Simulations are performed for both fixed and wave conditions. For the former the symmetry condition is used on the surface with a homogeneous Neumann outlet. For the wave conditions two newly implemented conditions are used: a free-surface and a convective outlet.

Three inflow profiles are considered at the inlet: uniform, flood and ebb. All are based on a bulk velocity of $1.5\,m/s$ with the latter two using velocity and turbulence intensity profiles fitted to measured data from the ADCP deployment TGL1A (see MD6.1). In all cases:

$$\underline{u} = (1.5, 0, 0) \tag{38}$$

$$k = \frac{3}{2}\underline{u}^2 I^2 \tag{39}$$

$$\omega = \frac{C_\mu^{-1/4} k^{1/2}}{l_m} \tag{40}$$

$$I = 10\% \tag{41}$$

$\underline{u}$ is the velocity vector, k the turbulent kinetic energy, ω the specific rate of dissipation, I the turbulence intensity. $C_\mu = 0.09$ is a constant and l_m a length-scale which is set to be 0.7 times the hub-height as specified in Gant and Stallard (2008).

5.2.2 Flow past the TGL 1MW turbine without waves

In order to assess the influence of turbulence and waves, simulations are first performed for a uniform inflow velocity with a rigid lid, slip boundary defined at the upper surface of the domain. The simulation is performed on the University of Manchester's CSF with a time-step of 1×10^{-2}s, equivalent to 3.6^o of rotation per second.

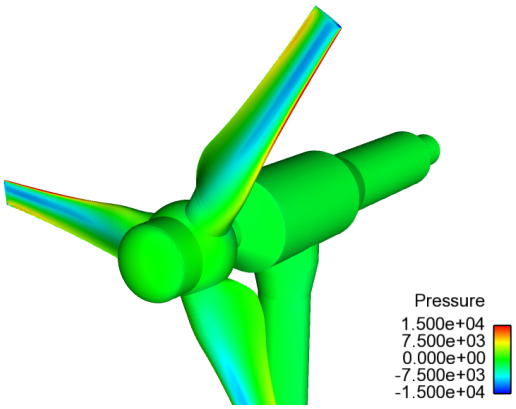

(a) Pressure distribution on the blades.

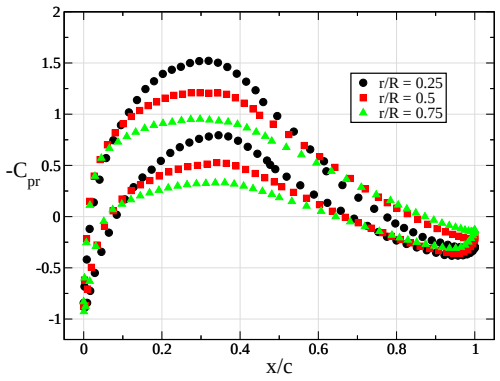

(b) Pressure coefficient on the blade at quarter length intervals.

Figure 29: Pressure distribution on the blades of the TGL 1MW turbine.

Pressure on the turbine blades, nacelle and mast are shown in 29a. Large pressure forces are observed on the blades as opposed to the rest of the turbine. The pressure coefficient is defined as:

$$C_{pr} = \frac{p - p_{ref}}{0.5\rho(U_O^2 + \Omega^2 r^2)} \tag{42}$$

Where p is the pressure, p_{ref} a reference pressure, here taken at the point of the inlet, and r is the radial distance from the origin. Fig. 29b shows the pressure coefficient at quarter lengths along the blade. As expected there is a large force on the suction side of the blade. There is also a smaller suction force on the underside of the blade towards the leading edge, which is visible as the blue area of the blade in Fig. 29a. As the behaviour at $r/R = 0.5$ and 0.75 is of similar shape to the performance characteristics of traditional hydrofoil shapes this is likely to be a result of the choice of reference pressure meaning that the values are off-set from zero. The irregular profile of the pressure coefficient at the root could be due to the blade at this section being built for strength rather than hydrodynamic performance. To validate and improve confidence in these results it may be useful to compare with 2D predictions of pressure coefficient that correspond to the lift and drag coefficients used in the rotor design tools GH Tidal Bladed and QBlade.

5.2.3 Effects in the near and far-field flow

Fig. 30 shows the instantaneous flow-field for the velocity, pressure and turbulent kinetic energy. For each variable the full length of the domain is shown illustrating the extent of the down-stream wake and the effect of the turbine on the approach flow. A close up of the flow in a plane around the blade and nacelle (shaded black) also describes the near-blade features. For the velocity the wake expansion goes beyond the rotor diameter and extends for almost the full length of the domain. The effect of the nacelle is seen clearly by a large velocity deficit in the centre-line away from the nacelle whilst there is also a large region of low velocity where the mast reaches the sea-bed. In the region above the swept area of the rotor plane there is an increased velocity due to blockage. This is an area that could change significantly when the free-surface is activated. As expected there are high velocities around the blade. Tip vortices are also clearly visible extending outward as the wake expands. The axial velocity in the whole region behind the blade is around two-thirds of the inflow velocity.

A high-pressure region is visible in front of the turbine (see Fig. 30b), which is extremely large compared to the pressure difference across the channel. As described above there is a large pressure change over the blade. Whilst the suction surface has a quite even distribution along the

	C_P	C_T
Current work	0.442	0.870
Current work - blockage correction ratio 3%	0.401	0.815
Original model - GH tidal bladed	0.457	0.799
Better definition - GH tidal bladed	0.438	0.794
Better definition - Qblade	0.425	0.788

Table 7: Averaged power and thrust coefficients for present simulations compared with TGL predictions. In the case of current work with blockage correction the corrected TSR is $TSR = 5.81$

chord-length the pressure side is largely focussed towards the tip region that could lead to uneven loading. As previously stated this should be investigated further.

Fig. 30c shows how the mast is responsible for a large area of TIKE at the mid-point between the channel-bed and hub-height. Despite this large area of interaction the wake below and above the hub-height are quite symmetrical. That behind the mast extends slightly further although the mast can be seen to have little effect on the wake in comparison to the mast. Behind the plane contours of lower regions of TIKE are observed that are related to the blade passing.

Wake profiles are shown for the normalised velocity and TIKE in Fig. (31). The effect of the mast appears small compared to that of the turbine blades. Indeed the no-slip condition on the channel-bed appears to have more effect on the profiles, which, for the velocity, start to show a developing shape of a profile. As previously mentioned the velocity above the turbine increases as it passes and here it is observed to slow to the reference velocity after $9D$.

Whilst the velocity in the centre-line recovers at further distances down-stream the TIKE is quite low up to $3D$ before increasing considerably at 5 and 7 diameters. In the area behind the tip the TIKE is extremely high in the near-wake. It can be observed that whilst the channel-bed is having some effect on the velocity field, the effect on the TIKE is much larger and this interferes in the rest of the profile considerably.

5.2.4 Turbine performance

Instantaneous power and thrust coefficients are shown in Fig. (32). As with the simulations for the Southampton turbine (MD1.2) these force coefficients fall steadily until the flow from the inlet reaches the turbine, here at 60 seconds. The coefficients begin to stabilise as the flow passes over the rotor reaching a periodic solution as the flow reaches the end of the domain. The coefficients are averaged over the last 30 seconds of physical time and compared to TGL predictions in Table (7). The current prediction of power is close to those provided by TGL, it is slightly higher than those for the better definition of the model, which is acceptable for these initial calculations. On the other hand the blockage corrected data, obtained with a blockage correction ratio of 3% and accordingly to Bahaj et al. (2007), shows a opposite trend with a C_T relatively close to the reference data and C_P slightly underestimated. Further investigations are on going in order to identify the cause of the discrepancy between the present CFD predictions and existing predictions of performance and loading.

5.3 Regular wave past a marine turbine

The second stage of this analysis is to investigate effects of waves on the turbine performance and loading. The procedure used in these simulations is the same as has been tested in the case of waves passing over a rotating cylinder and presented in Sec. 4. As already mentioned in the rotating cylinder the mesh is considered in two parts either side of a user defined limit (depth). Under this limit, the mesh is kept fixed with the obvious exception of the rotating cylinder containing the rotor. This limit is placed at a depth of $22\,m$ from the bottom surface, which correspond to

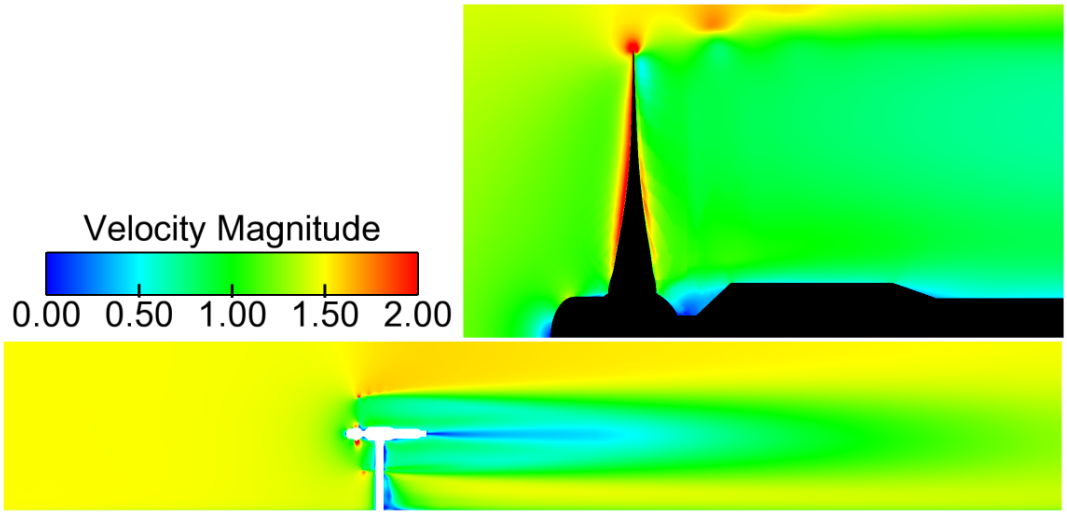

(a) Velocity.

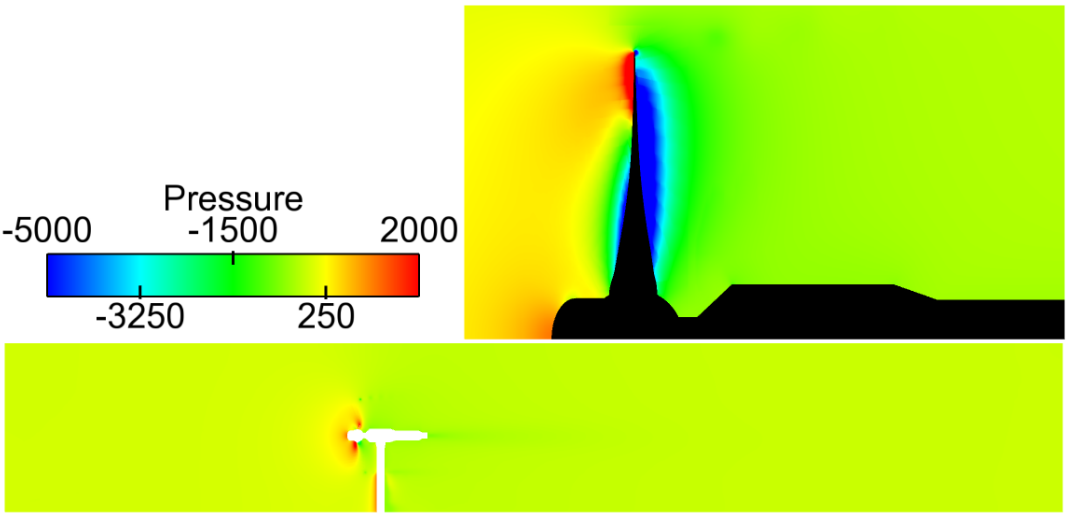

(b) Pressure.

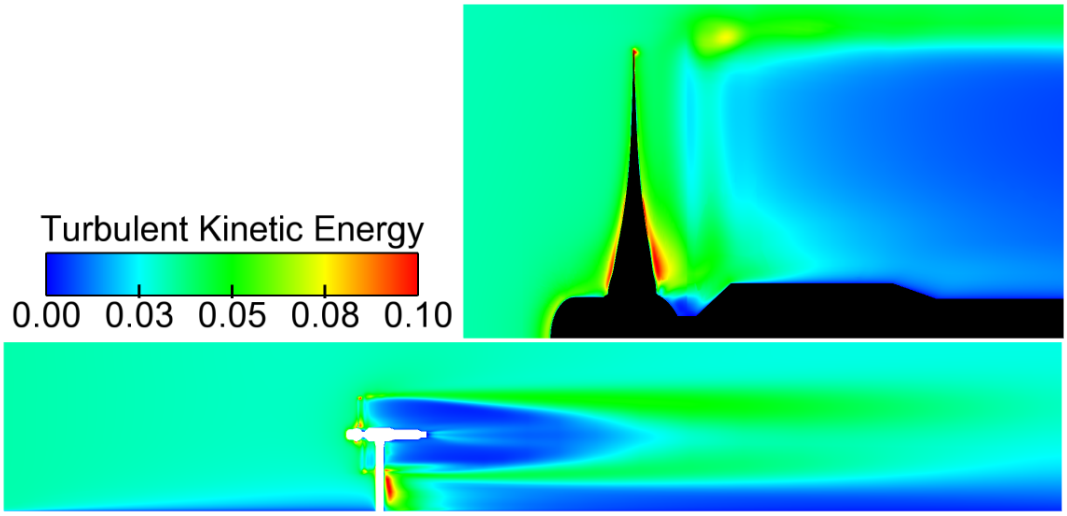

(c) Turbulent kinetic energy.

Figure 30: Flow field for different variables. In each case a plane through the length of the domain is shown as well as a close-up of the region around the blade and nacelle.

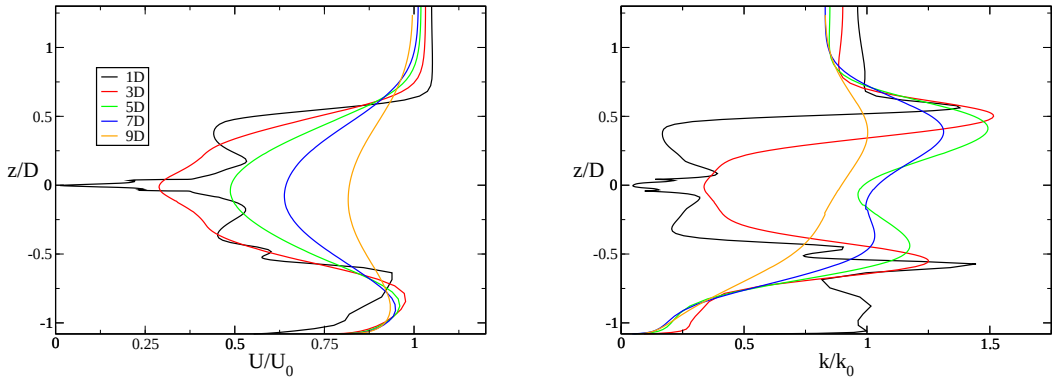

(a) Velocity: normalised by $U_0 = 1.5\,m/s$.

(b) TKE: Normalised by k_0 = inflow value as specified in Eq. (39).

Figure 31: Depth profiles in the wake, shown at 1 diameter and 2 diameter intervals thereafter.

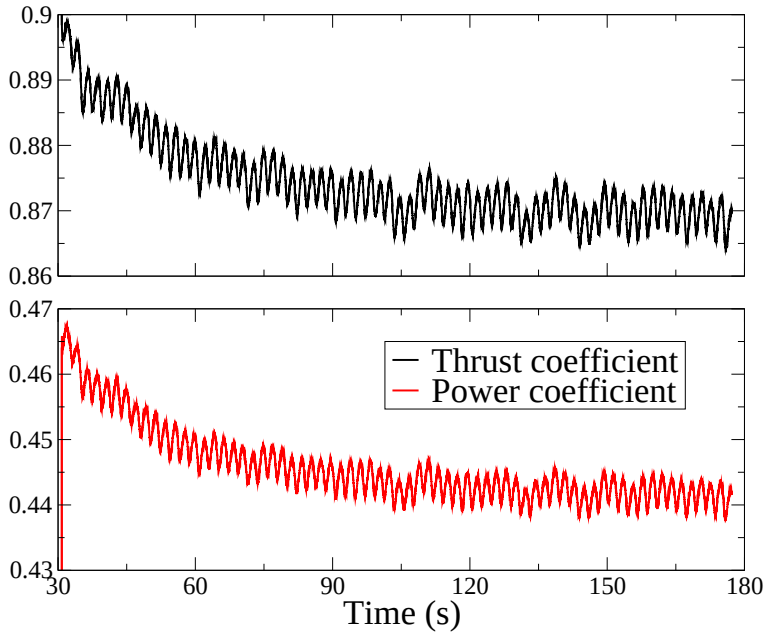

Figure 32: Uniform flow past 1MW turbine: instantaneous thrust and power coefficients.

	Wave1	Wave2
Water depth d	$43\,m$	$43\,m$
Amplitude A	3% of d	3% of d
Inlet Velocity U	$1.5\,m/s$	$1.5\,m/s$
Relative Period T'	$10\,s$	$7\,s$
Absolute period T	$9.08\,s$	$6.15\ s$
Celerity c	$16.67\,m/s$	$12.50\,m/s$
Froude Fr	0.09	0.12
Wave length λ	$148\,m$	$76.38\,m$

Table 8: Wave parameters definition for the regular wave over the TGL turbine.

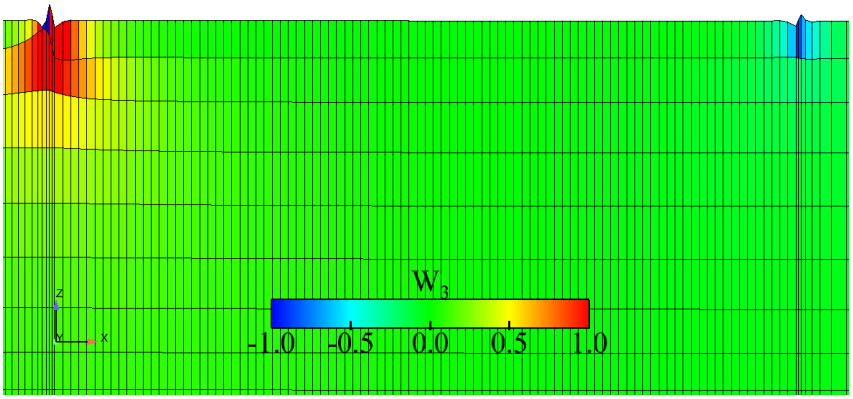

Figure 33: Mesh and vertical component of the mesh velocity w_3 close to the free surface for the mesh 4.2M.

$13\,m$ away from the turbine, centre of rotation, $4\,m$ from the blade tip, and $3\,m$ away from the sliding mesh interface. As for the rotating cylinder three different configuration are tested: one with free surface active, but no wave imposed at the inlet, and two different waves representative of the EMEC site conditions (see Table 8 for complete wave definition).

Free surface calculations without wave have been performed on the mesh described in Sec. 5.1. However, this results in a early stop after several hundred iterations only. The cause of the problem is visible in Fig. 33, where it is very clear that a problem has occurred on resolution of the vertical component of the mesh velocity (w_3). The reason for this erratic behaviour can be ascribed to the jump in the node distribution in the stream-wise direction due to the interface between two adjacent blocks. The problem has been generated by the projection of inner blocks, where the turbine is located and consequently the mesh is very fine on the outer domain. Indeed in the no-free-surface calculations this is not an issue since it occurs in the far-away domain where the flow field is unperturbed.

A new mesh for the outer domain including the lower stationary mesh and upper ALE mesh has, consequently, been built to correct the problem and also to increase the mesh density in the ALE region. Pressure and velocity fields with Wave1 ($Fr = 0.09$) and Wave2 ($Fr = 0.12$) are reported in Figs. 34 and 35 respectively. As already observed in the case of the rotating cylinder underneath a wave the turbine is subject to pressure waves. Indeed the velocity on the upper part of the domain is no longer uniform, but the wave induced velocity combined with the mean current results in variation from 1.25 to 2.25 m/s along the free surface. The quantitative results, specifically C_T and C_P time-history are reported in Fig. 36. The effect of the wave on the turbine performances is again analogue to the one observed for the cylinder. The longer wave (i.e. smaller

	C_P	C_T
Free surface only (Mesh 5.3M)	0.517	0.938
Wave1 $Fr = 0.09$ (Mesh 5.3M)	0.510	0.915
Wave2 $Fr = 0.12$ (Mesh 5.3M)	0.490	0.920
Free surface only (Mesh 5.6M)	~ 0.436	~ 0.91

Table 9: Averaged power and thrust coefficients for the 1MW turbine with free surface activated and waves. In the case of mesh 5.6M C_P and C_T values are only first estimations since coefficients just started to oscillate around a fix point.

Froude number) has a larger impact on the turbine performances, increasing the amplitude of both thrust and power coefficients. It is interesting to observe that time history profiles, for both C_P and C_T, approach sinusoidal and the period is of the order of T (absolute period).

Table 9 gives the average values for both C_T and C_P for simulations with a free surface represented by the ALE method and both without and with waves. Comparing the results with the ones in Table 7 it is obvious that the present simulation on the mesh with 5.3M control volumes overestimate both coefficients compared to TGL predictions. This might be a consequence of large pressure and velocity fluctuations arising in skewed area located around the rotor (both beside, see Fig.37, and in front of the rotor), below the upper moving part of the domain. Indeed from the figure is also obvious that these fluctuations are influencing the free surface where the mesh starts to be highly distorted. As a consequence the free surface calculation is stable for about $60\,s$ of physical time (around 8000 iterations) and the Wave1 for $22\,s$ of physical time (around 3000 iterations) and in both cases the calculation stops because of negative volume in the same area that has been already identify in the mesh 4.2M as critical. The calculation with Wave2 is, on the other hand, stable since the numerics has been modified in order to make stable the ALE module. Lower residual has been used for the resolution of the linear system and some of the options that usually employed in LES (i.e. reconstruction of the RHS in the resolution of the linear system) have been used. But, despite the calculation being stable and the mesh movement in the upper region begin more regular, the above mentioned checker-boarding oscillations are not completely removed.

For this reason a third mesh has been created with higher resolution in the ALE and an improved overall quality in the upper part of the domain, resulting in a total of $5.6 \cdot 10^6$ control volumes. In this case the mesh does not show checker-boarding oscillations. Indeed, this calculation has been started with a free-surface boundary condition of the top and it has been stable and the moving part of the mesh smooth for more than 10000 iteration. The differences between 5.3M and 5.6M are not very obvious (the distance between the free surface and the first layer of cell centres has been reduced, some few cells have been added in the top moving part and in the area immediately below, the orthogonality of the skewed area has been improved), but are fundamental in order to improve stability and results. As a confirmation of the improved performances of mesh 5.6M is not only the vanishing of the pressure oscillations but also the fact that C_T and C_P are approaching the values obtained in Sec. 5.2.4 (see Fig. 39). However, these values need to be confirmed since the flow field has only just established.

The main problem of this stage of the analysis is the computational time required for these simulations. Almost four days are necessary to perform the $200\,s$ of physical time required for one flow through of the domain. A half flow through (2 days) is required to establish whether a mesh is suitable for stable simulation and two flow-throw periods are preferable to establish and analyse a periodic solution. This estimation is valid for both HeCTOR (calculations performed on 512 processors) and EDF BlueGene (2048 processors). Therefore the process of verification of any change done in order to obtain a more stable and reliable result is presently extremely time consuming.

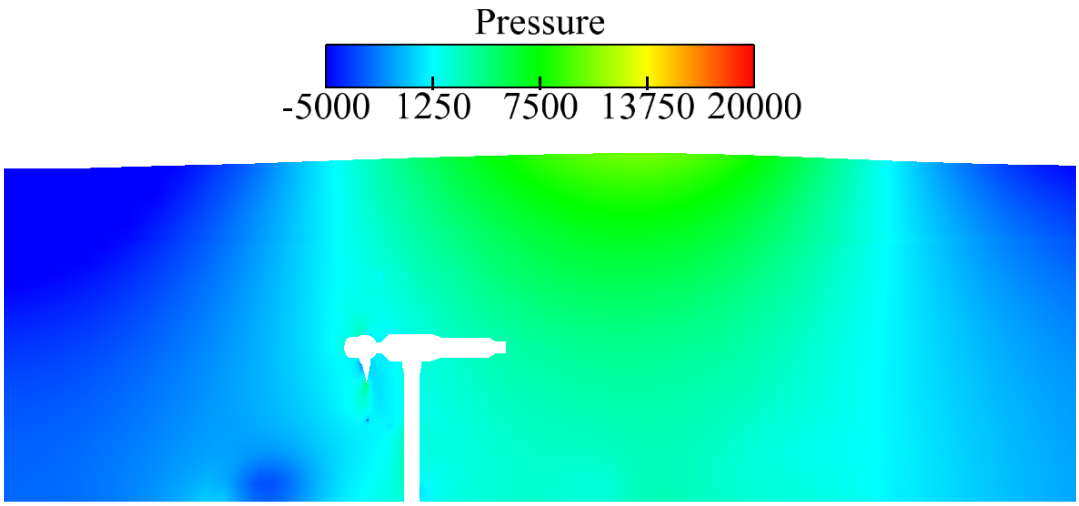

(a) Pressure.

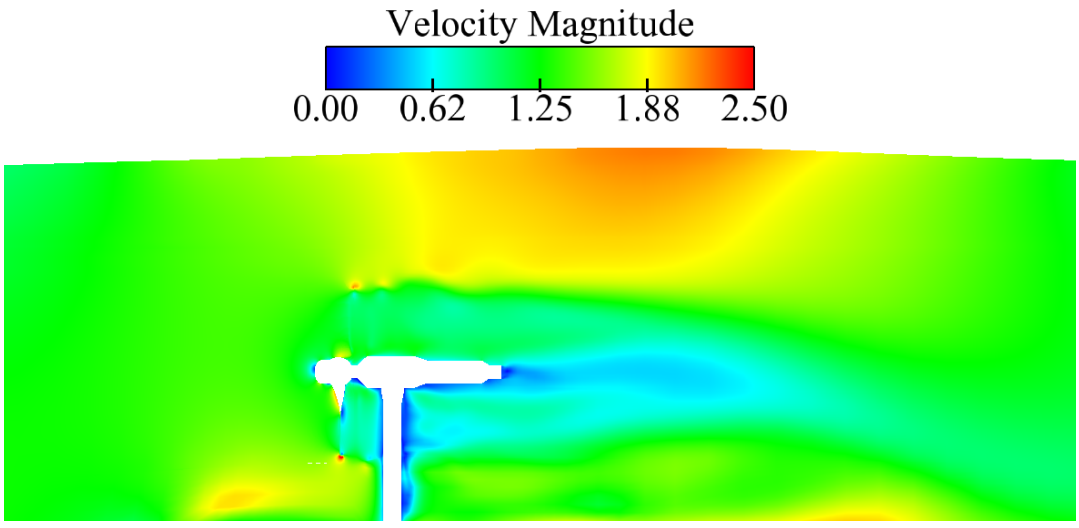

(b) Velocity.

Figure 34: Flow field around the TGL with Wave1 on the top ($Fr = 0.09$).

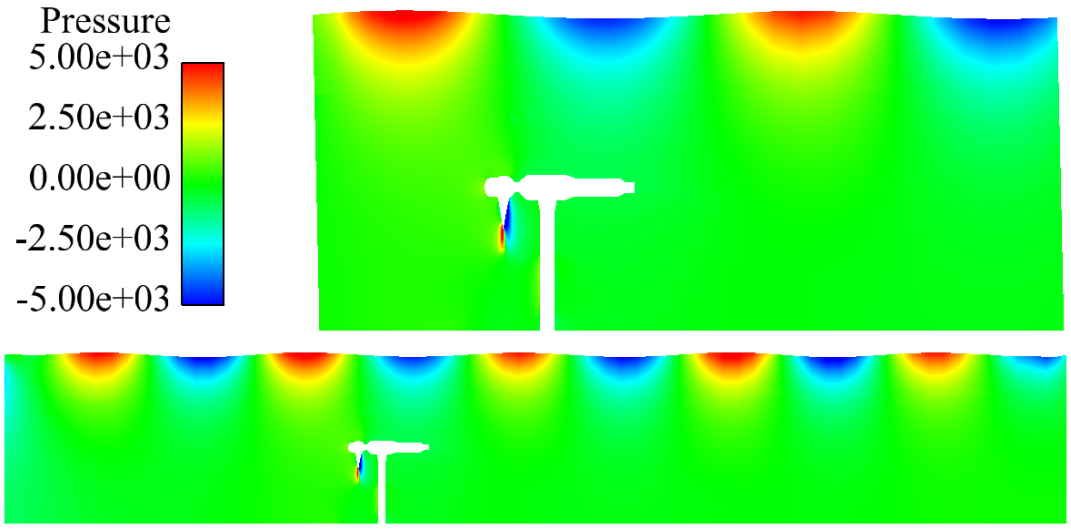

(a) Pressure.

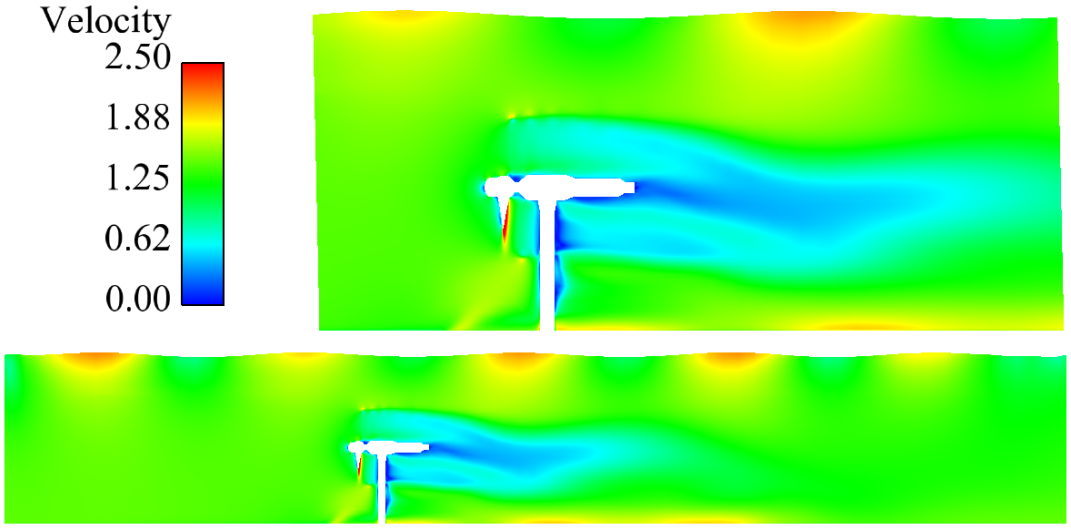

(b) Velocity.

Figure 35: Flow field around the TGL with Wave2 on the top ($Fr = 0.12$).

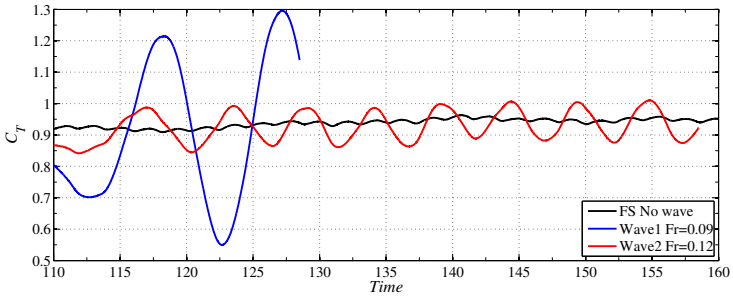

(a) Thrust.

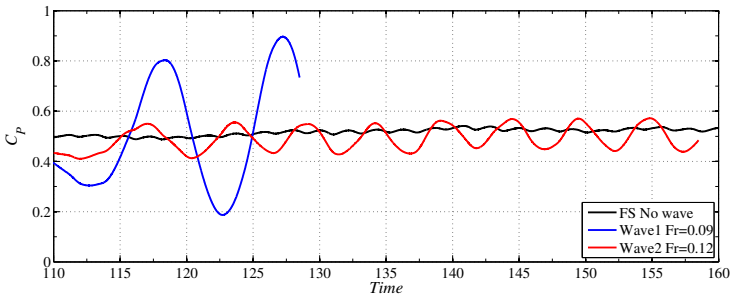

(b) Power.

Figure 36: Waves past 1MW turbine for the mesh 5.3M: instantaneous coefficients.

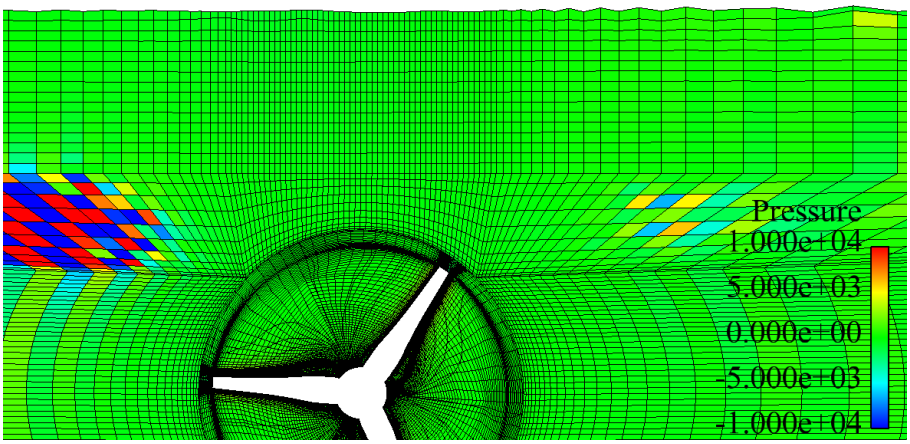

Figure 37: Instantaneous pressure for the 1MW turbine for the mesh 5.3M and and Wave1 on the top.

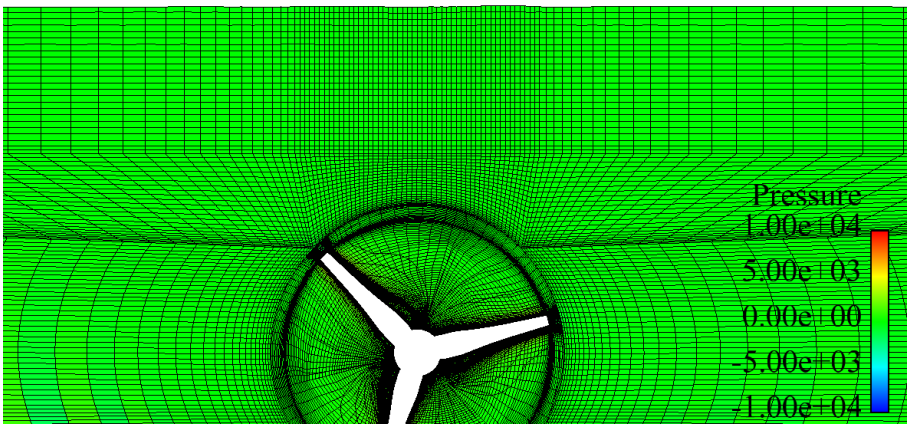

Figure 38: Instantaneous pressure for the 1MW turbine for the mesh 5.6M and free-surface on the top.

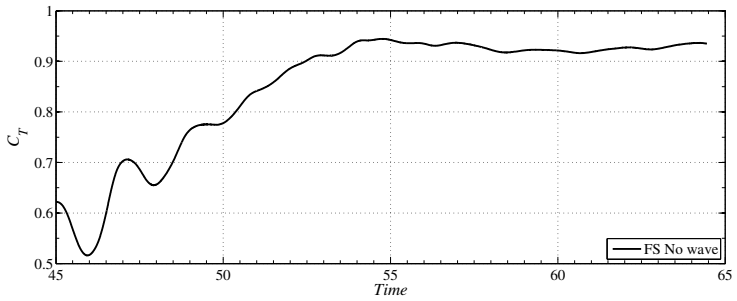

(a) Thrust.

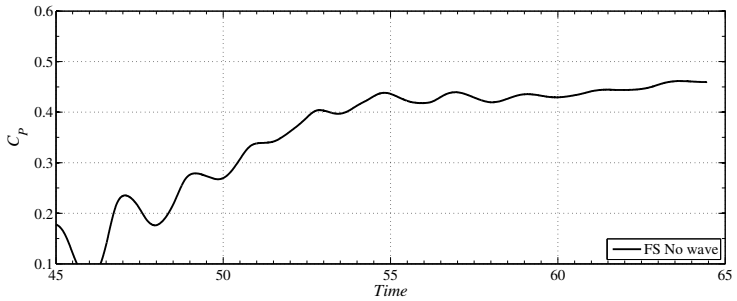

(b) Power.

Figure 39: Waves past 1MW turbine for mesh 5.6M: instantaneous coefficients.

5.4 Summary and Next Steps

Several developments have been made to *Code_Saturne* V_2.0 to improve the stability and computational efficiency of the ALE free surface method. This has been achieved by incorporating developments from V_2.2. The loading and wake of the TGL 1 MW turbine has been simulated using a RANS CFD method with a rigid-lid, a free surface modelled by ALE and imposed regular waves modelled by ALE. Simulations with a rigid lid predict power and thrust coefficients similar to existing predictions. The simulations of the turbine with imposed regular waves are stable, but presents some issues:

1. Spurious oscillations on the free-surface at the inlet. This was observed during 2D studies of regular wave propagation (see Secs. 2.3.1 and 2.3.2) on current and imposes a limit on the wave steepness that can be simulated. During 3D simulations with the turbine, these oscillations are larger;

2. Mesh distortion at the base of the ALE region where the moving mesh interfaces with the fixed mesh regions that contain the sliding mesh region. In the stream-wise direction the mesh density varies considerably along this interface resulting in some cells with slender aspect ratio;

All these issues are directly related to the present capabilities of the ALE module when implemented on a mesh of the form employed here. The problem of inlet spurious oscillations has been observed in all versions of the ALE module, but is most pronounced in the 3D turbine case with waves. One approach to resolving this issue may be to impose source terms in the first few cells down-stream the inlet, rather than having a Dirichlet condition on the inlet surface. The other problems are expected to become less severe with modification of the mesh structure and resolution. Mesh skewness, aspect ratio and the rate of stretching appear to be more particularly important. Further studies are ongoing to identify acceptable mesh for the ALE region and the interface with the stationary region. For this purpose the test-case of the submerged cylinder will be used in order to find some indications about suitable levels of skewing and stretching for the stability of the ALE module. Following this study an improved ALE mesh region will be developed in order to improve the results already obtained.

Much greater mesh resolution is a mandatory requirement for the LES calculations programmed for MD1.4 both in the upstream and downstream regions in order to properly resolve the incoming turbulent flow. For these simulations, turbulent inflow will be generated using the divergence-free Synthetic Eddy Method (div-SEM) proposed by Poletto et al. (2011). Therefore the mesh constraints imposed by the LES, are expected to be more onerous than those for the ALE module.

6 Future directions

The objective of the CFD work within ReDAPT is to assess the accuracy with which unsteady loads may be predicted. The MD1.3 simulations have shown that the TGL 1 MW turbine geometry has been simulated using RANS in a uniform flow and waves that are of similar magnitude to the EMEC deployment site. The objective of the MD1.4 simulations is to provide a more detailed simulation of the EMEC flow in order to assess the accuracy of unsteady load predictions. Representative data concerning both the EMEC flow and the TGL 1 MW turbine loading is required to complete this work. A summary is given in Section 6.1. In terms of simulation method the main difference to the present study is that LES will be employed. In addition the both a velocity profile and inflow turbulence will be defined at the inlet. A brief outline of the approach for defining the inflow conditions is given in Sections 6.2 and 6.3.

6.1 Representative Flow and Machine Data

Inputs to the MD1.4 simulations will include definition of the depth profile of velocity and of turbulence characteristics such as turbulence intensity and length scale and representative wave conditions. These inputs will be based on i) analysis of existing ADCP data from near the deployment site such as already completed to obtain depth profiles, ii) information on depth profile variation in the vicinity of the deployment site reported by MD5, iii) detailed flow measurements provided by MD3 from 500 kW turbine deployment and iv) detailed flow measurements provided by MD3 from 1 MW turbine deployment. A specification for the flow measurements required to obtain the necessary flow parameters is in development by University of Edinburgh (MD3) and University of Manchester (TGL Test Request Note 316).

Outputs from the MD1.4 simulations will focus on unsteady loading but will also include details of the near wake. Predicted loads will be compared to measurements from the TGL 1 MW turbine. The mean flow speeds that will be simulated are partly dependent on the availability of data for comparison. A specification of the required load measurements, and near-wake measurements, has been defined by University of Manchester and University of Edinburgh (TGL Test Request Note 317).

6.2 Definition of Inlet Profile

As well as the uniform profile that has been used in the current simulations, profiles for the velocity and turbulence intensity will be specified at the inlet that matches those of the EMEC test site. Both flood and ebb profiles, based on a bulk velocity of $1.5\,m/s$, will be prescribed by data from MD6.1. For these:

$$\underline{u} = (U(x_3), 0, 0) \tag{43}$$

$$k = \frac{3}{2}\underline{u}^2 I^2 \tag{44}$$

$$\omega = \frac{C_\mu^{-1/4} k^{1/2}}{l_m} \tag{45}$$

$$I = zo10\% \tag{46}$$

Flood As suggested in MD6.1 a power law is used for the velocity profile. For I a polynomial is fitted to the data points for the $1.5\,m/s$ flow conditions in MD6.1.

$$U(x_3) = u_{ref}\left(\frac{x_3 + x_{3hub}}{x_{3ref}}\right)^{\alpha}$$

$$I(x_3) = \sum_{i=0}^{n} A_i x_3^i$$

The values of $\alpha, u_{ref}, z_{hub}, z_{ref}$ and $A_i's$ are in Ebb and the profiles are shown in Ebb.

Ebb Polynomials are fitted to the data points for the $1.5\,m/s$ flow condition in MD6.1 for both velocity and turbulence intensity.

$$U\left(x_3\right) = \sum_{i=0}^{n} A_i x_3^i$$

$$I\left(x_3\right) = \sum_{i=0}^{n} A_i x_3^i$$

Again the values of $A_i's$ are in Ebb and the profiles in Ebb.

Profile	α	u_{ref}	z_{hub}	z_{ref}		
Flood velocity	0.14	1.5	19.5	15		
	n	A_0	A_1	A_2	A_3	A_4
Ebb velocity	2	1.643	0.006	-8.81E-4		
Flood I	3	9.438	-0.403	0.011	3.15E-4	
Ebb I	4	8.925	-0.193	0.036	3.81E-4	-4.70E-5

Table 10: Coefficients used for the power-law and polynomial profiles fitted to velocity and turbulence intensity (TI) data sets from MD6.1.

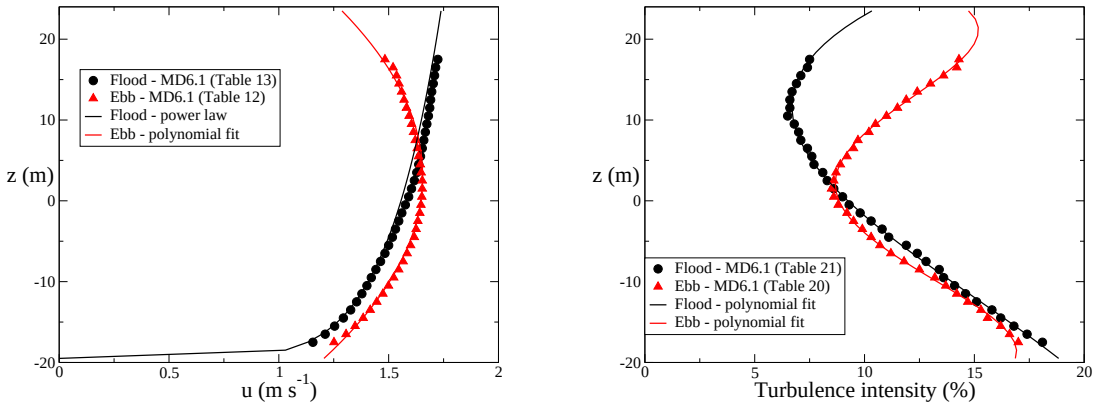

Figure 40: Profiles fitted to EMEC data. Left velocity, right turbulence intensity. See Ebb for coefficients.

Similar polynomial fit analysis has been conducted for a range of mean flows within ReDAPT MD5.2 (Due Jul 2012). This information will be employed where possible.

6.3 Definition of inflow turbulence in LES

The correct simulation of turbulent conditions in the LES calculations will require the implementation of a method in order to reconstruct turbulent fluctuations at the inlet. This will be achieved implementing in *Code_Saturne* a divergence-free synthetic eddy method (DF-SEM) as proposed by Poletto et al. (2011). As already mentioned a work on the refinement of the mesh is mandatory in order to properly resolve the wake behind the turbine and to have enough resolution downstream the inlet in order to sustain the turbulent fluctuations generated with the SEM. Preliminary indications suggest that mesh resolution will increase by a factor of 2 or 3, therefore the mesh size

will be of the order of $10 \cdot 10^6$ and $15 \cdot 10^6$ control volumes. Simulations will be performed on the HeCTOR super-computer for which the project has been awarded computational resources and some preliminary results are expected by the beginning of October.

References

Archambeau, F., N. Mechitoua, and M. Sakiz (2004). Code_Saturne: a finite volume code for the computation of turbulent incompressible flows - Industrial Applications. *Int. J. Finite Vol. 1*(1).

Bahaj, A. S., A. F. Molland, J. R. Chaplin, and W. M. J. Batten (2007). Power and thrust measurements of marine current turbines under various hydrodynamic flow conditions in a cavitation tunnel and a towing tank. *Renewable Energy 32*(3), 407–426.

Cheng, M., Q. Yao, and L.-S. Luo (2006). Simulation of flow past a rotating circular cylinder near a plane wall. *International Journal of Computational Fluid Dynamics 20*(6), 391–400.

Cozzi, O. (2010). Free surface flow simulation: correcting and benchmarking the ALE method in Code_Saturne. Master's thesis, University of Manchester, School of MACE.

Dean, R. G. and R. A. Dalrymple (1991). *Water wave mechanics for engineers and scientists*, Volume 2 of *Advance series on Ocean Engineering*. World Scientific Pub Co Inc.

Ferrand, M. (2011). Couplage des composantes de vitesse dans code_saturne. adaptation du module ale et application aux écoulements à surface libre. Internal report H-I83-2011-02272-FR, EDF R&D.

Ferziger, J. H. and M. Peric (1997). *Computational Methods for Fluid Dynamics*. Springer.

Gant, S. and T. Stallard (2008). Modelling a Tidal Turbine in Unsteady Flow. In *Proceedings of the Eighteenth (2008) International Offshore and Polar Engineering Conference*, Number 2007, pp. 473–479.

Gingold, R. A. and J. J. Monaghan (1977, November). Smoothed particle hydrodynamics - Theory and application to non-spherical stars. *Monthly Notices of the Royal Astronomical Society 181*, 375–389.

Harlow, F. H. and J. E. Welch (1965). Numerical Calculation of Time-Dependent Viscous Incompressible Flow of Fluid with Free Surface. *Physics of Fluids 8*(12), 2182–2189.

Hirt, C. and B. Nichols (1981). Volume of fluid (VOF) method for the dynamics of free boundaries. *Journal of Computational Physics 39*(1), 201 – 225.

Mayer, S., A. Garapon, and L. S. Sorensen (1998). A fractional step method for unsteady free-surface flow with applications to non-linear wave dynamics. *International Journal for Numerical Methods in Fluids 28*(2), 293–315.

Mittal, S. and B. Kumar (2003, March). Flow past a rotating cylinder. *Journal of Fluid Mechanics 476*, 303–334.

Poletto, R., A. Revell, T. Craft, and N. Jarrin (2011). Divergence free synthetic eddy method for embedded LES inflow boundary conditions. In *Seventh International Symposium On Turbulence and Shear Flow Phenomena (TSFP-7)*, Ottawa.

Russell, J. (1844). Report on waves. In *14th meeting of the British Association for the Advancement of Science*, pp. 311–390.

Thé, J. L., G. D. Raithby, and G. D. Stubley (1994). Surface-adaptive finite-volume method for solving free surface flows. *Numerical Heat Transfer, Part B: Fundamentals 26*(4), 367–380.